***Highlights**

- Lungmu Co (west Tibet) mafic rocks and granite resulting from Cretaceous Jinsha subduction.
- Cooling in the early Upper Cretaceous and final exhumation in Paleocene.
- Paleocene NW Tibet uplift as a far field effect of India/Eurasia collision.

*Graphical Abstract

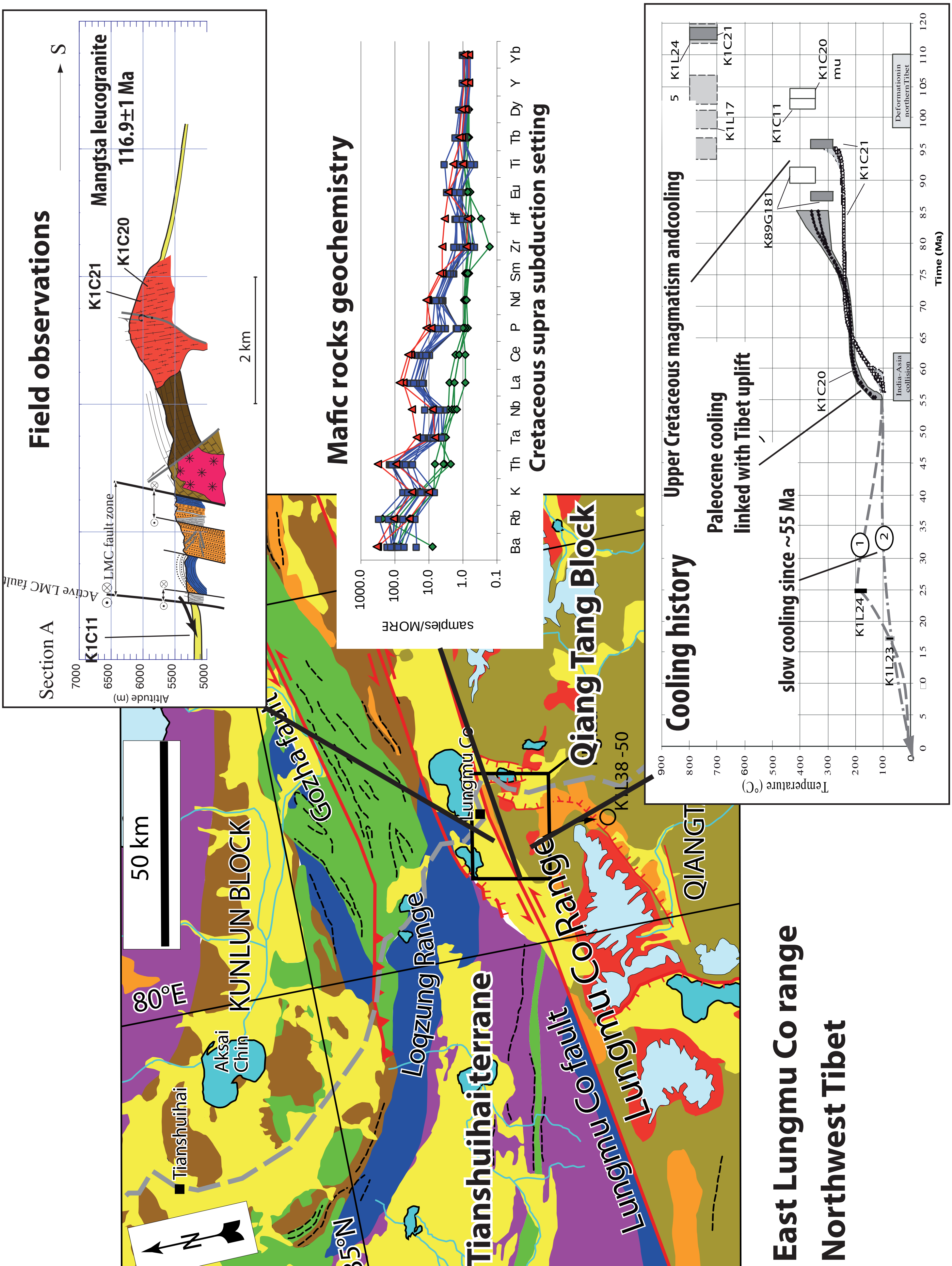

Successive deformation episodes along the Lungmu Co zone, west-central Tibet.

Leloup P.H.[1], Arnaud N.O.[2], Mahéo G.[1], Paquette J.L.[3], Guillot, S.[4], Valli F. [5], Li H.[5 &6], Xu Z.[6], Lacassin R.[5], and Tapponnier P. [5].

1 : Laboratoire de Géologie de Lyon: Terre, Planètes et Environnement, UMR CNRS 5276, Université Claude Bernard – Ecole normale supérieure de lyon, 2 rue Raphaël Dubois, 69622 Villeurbanne, France.
herve.leloup@univ-lyon1.fr
2: ISTEEM-UM2, Géosciences Montpellier, UMR CNRS 5243, Université des sciences et techniques du Languedoc, 4095 Montpellier cedex 5, France.
3: Laboratoire Magmas et Volcans, UMR CNRS 6524, Observatoire de Physique du globe de Clermont-Ferrand, 63038 Clermont-Ferrand, France.
4 : ISTerre, CNRS, University of Grenoble I, BP 53, 1381 rue de la Piscine, 38041 Grenoble cedex 9, France.
5 : Equipe de Tectonique, Institut de Physique du Globe de Paris, Sorbonne Paris Cité, Univ Paris Diderot, UMR 7154 CNRS, F-75005 Paris, France.
6: Institute of Geology, CAGS, 26 Baiwanzhuang Road, Beijing 100037, PRC

Abstract

Field study, thermochronology and geochemistry of the east Lungmu Co (LMC) range highlight some of the geological events that shaped western Tibet. The LMC fault zone has long been interpreted as the boundary between the Tianshuihai terrane of Laurasian affinity and the Qiangtang block of Gondwanian affinity. In the LMC range, the Paleozoic series is intruded by the Mangtsa leucogranite whose zircon have a U/Pb age of 116.9±1 Ma and by mafic rocks with U/Pb zircon ages ranging from 116.9±1 to 95.1±1.7 Ma. Geochemistry of the mafic rocks indicates that they have been emplaced in a supra-subduction zone setting, probably the north dipping Nujiang suture zone. $^{40}Ar/^{39}Ar$ micas ages of the granite indicate that cooling below ~350°C occurred between 105 and 85 Ma. $^{40}Ar/^{39}Ar$ K-feldspar data suggest a fast cooling event at 60-55 Ma, which we relate to the reactivation of the LMC suture zone as a thrust at the onset of the India – Eurasia collision. The last, and still active, deformation event corresponds to left-lateral strike-slip faulting along the ENE-WSW LMC fault.

1 Introduction

Tibet, the highest and largest topographic plateau on earth, was essentially built during the Cenozoic (e.g., Harrison et al., 1992; Tapponnier et al., 2001). However, the precise timing and mechanisms of the plateau building remain highly debated. This is in part because the long geological history of Tibet is still poorly known especially in remote area such as central and western Tibet. In western Tibet, the highest part of the plateau at more than 5000m asl, essential information such as detailed stratigraphy, continuity of known sutures, offset of those structures by major faults and geochronological constraints are still lacking. In this paper we aim to present new structural, geochronological and geochemical data from the Lungmu Co range in west-central Tibet (Fig. 1).

The Lungmu Co (LMC) range is a noticeable topographic ridge culminating at 6192m, located south of LMC lake that stands at an altitude of ~5100m (Fig. 2a). The northern flank of the range corresponds to the eastern extremity of the active left-lateral LMC fault that can be traced for more than 150 km towards the right-lateral Karakorum fault (Molnar & Tapponnier, 1977) (Fig. 1a). The Karakorum fault is interpreted as the western boundary of the Tibetan plateau but its precise initiation age, total offset and present day rate are still debated (e.g., Leloup et al., 2011; Robinson; 2010; Valli et al., 2008; Chevalier et al., 2005). The LMC fault appears to abut against the Karakorum fault, whilst it has been interpreted to offset that fault by ~27 km (Raterman et al, 2007). Towards the Northeast, strike-slip motion of the LMC appears to be transferred to the Gozha fault (Fig. 1b) that ultimately merges with the Altyn Tagh fault which bounds the Tibetan plateau to the north (Fig. 1a) (Molnar & Tapponnier, 1977; Peltzer & Saucier, 1996).

It has been proposed by Matte et al. (1996) that the LMC range also corresponds to the boundary between the Tianshuihai terrane to the north and the Qiangtang block to the south, marking the prolongation of the Triassic Jinsha suture (Fig. 1a).

The data presented herein document the geology of the LMC range shedding light on more than 300 Ma of its geological history and its role in plateau evolution.

2 Regional geology of the Lungmu Co area.

2.1 The Tianshuihai terrane

North of the LMC range, the Tianshuihai terrane is characterized by Carboniferous greenschists and greywackes overlain by Permo-Triasic flyshoïd dark slates (Matte et al., 1996). These series are unconformably capped by marine Jurassic black shales, and Cretaceous conglomerates, red sandstones and limestones (Fig. 1b).

South of the LMC range the Permo-Carboniferous series consists in black shales, Tethyan fusulinids bearing limestone and quartzite horizons. Presence of diamictites suggests a Gondwanian affinity (Matte et al., 1996). Further south, near Domar, the Permo-

Carboniferous series is overlain by Triassic conglomerates and Jurassic limestone, this latter being locally unconformably overlain by Cretaceaous-Paleocene sandstones and red conglomerates (Matte et al., 1996).

These stratigraphic differences have led several authors to propose that the LMC fault could correspond to the boundary between the Tianshuihai block to the north and the Qiantang block to the South (Matte et al., 1996; Norin, 1946; Sengör and Okurogullari, 1991) (Fig. 1a). In such interpretation, the Tianshuihai terrane would constitute, together with the Bayan Har and Songpan terranes, a large block bounded to the North by the South Kunlun suture, the trace of a north dipping Permo-Triassic subduction. South of this block, the LMC would be the western prolongation of the South dipping Triassic Jinsha suture described in central and eastern Tibet (e.g., Roger et al., 2003). However, no ultrabasites have been found in the LMC area and the detailed structure and thermal history of the range are unknown. Furthermore, the zone is sliced by recent strike-slip faults that may have disrupted the initial relationships between the units.

2.2 The Lungmu Co and Ghoza faults

The Ghoza - LMC strike-slip fault zone corresponds to two distinct faults that connect through an extension zone north of the LMC range at midway of its total length (Fig. 1b) (e.g., Liu et al., 1991). These faults are poorly documented from field observation, whilst some segments show clear morphological indications of left-lateral active shear (Fig. 3e) (e.g., Molnar & Tapponnier, 1977; Armijo et al., 1986; Liu et al., 1991; Raterman et al., 2007). From the apparent offset of geological formations seen on Landsat images, it has been proposed that the total LMC fault offset amount is of about 25 - 32km, and affects the Karakorum fault (Raterman et al., 2007). Axes of folds affecting the Cretaceous limestones trend NNW-SSE near Tianshuihai . This trend swings counter clockwise by 60° when approaching the LMC (Fig. 1b). If this bend is interpreted as due to fault-drag, it would suggests a minimum of ~50 km for the left-lateral offset.

3 The Lungmu Co range.

Our description of the Lungmu Co (LMC) range is based on two detailed field cross-sections (A & B, Fig. 2b), field observations around the range, and SPOT and Landsat ETM+ satellite image interpretation (Fig. 2a). Given the access difficulties some observations are based on rocks collected in streams coming down from the range (Fig. 1b; Fig. 2a).

3.1 Rock facies and general structure

The range encompasses two main granitoïd bodies, as well as some basaltic dykes. The sedimentary cover includes carbonates, a flyshoïd series, and a clastic series dominated by red sandstones. Bedding dips mostly to the N-NE in the core of the range and become almost vertical on the Northern flank (Fig. 2b; Fig 3b). In this zone, the sedimentary rocks are affected by several steeply dipping faults trending ENE-WSW. Locally such faults isolate calcshist slivers. One sliver shows cleavage trending N130 to N160 affected by numerous left-lateral shear planes trending N80 to N 120 and few right-lateral planes trending N130 to N145 (Fig 3d). In another sliver the cleavage trends N97 75 N on average with an almost horizontal lineation (pitch ~10° W) (Fig 3c). Such deformation probably results from strike-slip motion along the still-active LMC fault, thus defining a ~1.5 km wide left-lateral shear zone (Fig. 2; Fig. 3a). The red sandstones and conglomerates rest unconformably on black schists and some schistose conglomerates bear angular schist clasts, suggesting that several deformation events may have succeeded through time. The red sandstones, of Neogene age (N_{1-2}) according to the Tibet geological map (Chengdu Institute of Geology, 2004), are affected by normal faults that have been tilted together with the stratification (section A, Fig. 2b). They are are also found in the core of the range, resting unconformably on the flyshoïd series and overthrusted by dark grey fossiliferous limestones (section B, Fig. 2b). From regional stratigraphy the limestones are attributed to the Permian of the Qiangtang block. Further to the East, the limestones are intruded by leucogranites that show a steep E-W foliation. Towards the north the limestones are in a steep fault contact with dolomitic limestones that have been intruded by a granodiorite body. In map view, the thrusts appear to trend NE-SW and are bounded to the north by the LMC fault zone (Fig. 2a).

The flyshoïd series composed of the alternance of dark sandstone and slate, are affected by folds verging to the South and intruded by basaltic necks. From satellite image interpretation, similar series appear to occupy a wide area of the South LMC range (Fig. 2a). South of this zone outcrops a NW-SE elongated body mapped as βμJ on the geological map (Chengdu institute of geology and mineral resources, 2004). Rocks sampled at the western extremity of this body (K1L 16-18, Fig. 2a) are dacite and andesite. A river flowing out of the range (Fig. 2a) allowed us to sample paragneisses, orthogneisses, gabbros, diorite, andesite and basalt (samples K1L19 to 30).

3.2 Granitoids: relationships with stratigraphy and deformation.

A granodiorite body intrudes the dolomitic limestones and caused contact metamorphism and marble formation. The granodiorite and the dolomitic marbles are deformed both by the LMC fault zone to the North and by a reverse fault to the South (section A, Fig. 2b).

East of the LMC range stands the ~4x4 km MangTsa leucocratic granite (Fig. 2a). The granite is offset by the active normal faults bounding the LMC range to the east, and covered by quaternary deposits in its central part. The granite comprises quartz, perthitic K-feldspar, plagioclase (oligoclase, muscovite and subsolidus titano-magnetite surrounding biotite). Such petrology is indicative of a crustal origin. The granite is undeformed in its SE part (K89G181) and shows a steep ~E-W foliation to the NW (KC20 & KC21) (Fig. 2). Both plagioclase and K-Feldspar porphyroclasts commonly show recrystallized grains at their boundaries, producing a core-and-rim structure diagnostic of dynamic recrystallization. Observations in natural examples suggest that such dynamic recrystallization occurs at medium- to high-grade temperature conditions (400-600 °C) during deformation (Passchier and Trouw, 1996). Similarly quartz grains show dynamic recrystallization through subgrain rotation or grain boundary migration. These microstructures are typical at medium- to high-grade conditions (400-700°) (Passchier and Trouw, 1996). Mica fish also show flexuous shape, symptomatic of boudinage and recrystallization at the edges at temperature higher than 250 °C (Stesky, 1978). Thus, the foliation corresponds to a relatively high temperature (> 400°C) deformation. One sample (K1C11, sampled in moraines on the north side of the LMC range) developed a lower temperature deformation superimposed on the relatively HT foliation. This late deformation is characterized by the occurrence of secondary millimetric muscovite and kinking of the K-feldspar, quartz locally exhibit undulose extinctions typical of low-grade conditions below 300 °C (Passchier and Trouw, 1996). There is no evidence whether this deformation is only restricted to the granite or has a regional signification.

South of the LMC range, andalusite bearing samples K1L38, 42a and 50 (Fig. 1b) are related to contact metamorphism at ~500-550°C and ~2 – 3 kb (Hilairet, 2002). Such contact metamorphism probably occurred at the time of emplacement of the granites that can be seen on the landsat images (Fig. 2a). The same samples also show relict garnets and staurolite suggesting a previous metamorphic event with higher metamorphic conditions of 550-600°C and ~6Kb (Hilairet, 2002).

3.3 Mafic rocks: petrology and geochemistry.

A large mafic body is mapped from on the Landsat images SW of the flyshoïd series (Fig. 2a). Rocks sampled at the northern extremity of that body are dacite (samples K1L16 to 17). Other mafic rocks have been sampled as pebbles in a river bed further east, probably coming from the southern part of the mafic body (samples K1L19 to 30). They are basalt, diorite, dacite and amphibolitized diorite. The basalt (K1L27) presents altered clinopyroxene, microlite of plagioclase and ilmenite. Two types of diorites have been distinguished. Type A (K1L23, 22, 24, and 24b) are undeformed, medium grain, and contain green amphibole, plagioclase, ilmenite ± biotite + accessory minerals (apatite, monazite ± titanite). Biotite is a primary magmatic mineral and usually developed before the amphibole. Quartz is locally present (K1L24). Type B diorites (K1L29, 30, and 25a) do not contain any biotite nor accessory mineral. The dacites (K1L17, 26, 28a and 25b) are undeformed with a porphyritic texture characterized by magmatic amphibole, plagioclase and quartz ± biotite. All these samples are slightly retrogressed with the development of chlorite at the expense of biotite and amphibole, while plagioclases are partially sericitized. Amphibolitized diorites (K1L21, 28b, 47 and 48) show amphibole and plagioclase recrystallization under sub-solidus conditions. Secondary minerals are titanite, quartz, ilmenite and locally calcite (K1L47, K1L48). Chlorite is sparse suggesting temperature of recrystallization above 350°C.

In order to discuss the genesis of the mafic rocks, the chemical composition of 6 diorites (K1L22, 23, 24, 24b, 29 and 30), 1 basalt (K1L27) 4 dacites (K1L16, 17, 25 and 26) and 5 amphibolitized diorites (K1L21, 28b, 46, 47 and 48) has been measured. Major elements and some transition elements (Cu, Cr, V, Ni, Co, Sc) were analyzed by X-ray fluorescence at the University of Lyon. Other trace elements (Rb, Sr, Ba, Th, U, Pb, Y, Zr, Nb, Hf, Ta, Zn, and Rare Earth Elements) were analyzed by ICP-MS at the ENS of Lyon. Loss on ignition (LOI) was determined by heating the sample at 1000°C for 30 minutes. Analytical results are presented in Table 1.

SiO_2 and MgO contents of the samples range from 42.35 % (amphibolite) to 66.60% (dacite) and 1.20% (dacite) to 12.74% (amphibolite) respectively. All the samples have a low to medium content in K_2O, TiO_2 and Na_2O (0.48 – 3.99 %; 0.55 – 4.23%; 1.31-3.71% respectively) and medium to high concentration in CaO, Fe_2O_3, Al_2O_3 (3.34-15.06%; 4.06-15.79%; 9.05-19.85% respectively). Such chemical composition is characteristic of calc-alkaline to high-K calc-alkaline rocks. In plots of MgO, taken as a differentiation index, versus major elements (Fig. 4), all the major elements show either positive (SiO_2, Na_2O, K_2O,

Al_2O_3) or negative (TiO_2, CaO, FeO) correlation with differentiation. Such relationship suggests that all samples belong to the same fractionation trend.

Based on the REE patterns (Fig. 5) three groups can be defined. (1) Horizontal patterns characterized by a slight depletion or enrichment in light REE (LREE) relative to heavy REE (HREE) with $(La/Yb)_n$ ratios between 0.7 and 1.43. This group contains type B diorites and some amphibolitized diorite (K1l28b, 29, 30 and 48). (2) Steep patterns characterized by a strong enrichment in LREE relative to HREE with $(La/Yb)_n$ ratios between 10.7 and 24.8. This group consists in type A diorites (K1L22, 23 and 24), basalt (K1L27), dacites (K1L16, 17, 25b and 26) and some amphibolitized diorites (K1L21 and 46). (3) Steep patterns characterized by the strongest enrichment in LREE relative to HREE with $(La/Yb)_n$ ratios between 42.3 and 43.5. This group consists in one type A diorite (K1L24b) and one amphibolitized diorite (K1L47). The transition between the different group does not appears to be correlated with fractionation as MgO contents overlap (6.56 to 7.78 wt% for group 1, 1.2 to 11.98 wt% for group 2 and 4.75 to 12.74 wt% for group 3).

All MORB-normalized spidergrams (Fig. 5) are characterized by enrichment in Large Ion Lithophile Elements (LILE) such as Ba, Rb, Sr and K relative to REE and High Field Strength Elements (HFSE). HFSE show a slight depletion relative to REE for group (2) and (3) only. Despite a similar HFSE content, such relative depletion is not observed for group (1) samples as the LREE content is significantly lower than in groups (2) and (3) samples. Groups (2) and (3) are also characterized by a strong enrichment in Th not observed in group (1) samples for similar MgO content.

LILE enrichment results from different processes. As these elements are very mobile, they could have been enriched by re-mobilization during sea floor hydrothermalism or metamorphism related to obduction and/or collision. Alternatively, their enrichment could also suggest that the mantle source of these rocks had been either previously and selectively metasomatized in a supra-subduction zone context (Tatsumi et al., 1986) or contaminated by sediments or continental crust. Finally, such enrichment can be related with fractional crystallization. The secondary mobility of LILE (by example Sr) can be evaluated by plotting their concentration against that of less mobile elements (Fig. 6) such as REE (Nd, Pr). Two trends are observed. The samples with the lowest (but enriched compared to HFSE) LILE contents define a linear trend best explained by a fractional crystallization process. On the other hand, the samples with the highest LILE concentration are significantly shifted away from the fractional crystallization trend. Such a shift is indicative of secondary LILE re-mobilization probably during sea floor alteration or metamorphism. For the relatively less enriched samples (first trend), the LILE enrichment is primary. Effect of crustal contamination or fractional crystallization can be estimated by considering only the samples that lie along a fractional crystallization trend in the previous plots as other samples chemistry is modified by fluid circulation. Among these samples even the most primitive ones are highly enriched in LILE (SiO_2<52%). This observation is incompatible with fractional crystallization or crustal assimilation as the only factors controlling the LILE enrichment. However such processes could have contributed to the observed chemistry. Consequently the LILE enrichment observed in all samples is most probably related to the metasomatism of the mantle source in a supra-subduction zone context.

The differences between the three groups can be related with (1) fractional crystallization or (2) the existence of several metasomatized sources. As previously discussed, in plots of MgO versus major elements (Fig. 4) all the samples define the same fractionation trend. Differentiation by fractionation can be tested using plots of incompatible elements ratios versus compatible elements (i.e. V and Sc, Fig. 7). In such plot, compatible elements are taken as a differentiation index. Ratios between chosen incompatible elements usually do not change during partial melting or fractional crystallization, unless fractional crystallization or preferential melting of some peculiar mineral phases occurs. If such event takes place the incompatible elements ratio will change with differentiation index. In our plots, incompatible elements ratios for groups (2) and (3) samples does not significantly change with differentiation (Fig. 7). On the contrary groups (1) samples define steep lines characterized by progressive depletion in Th or LREE (Ce) relative to LILE (Rb), HFSE (Ta) or HREE (Dy), starting with the incompatible elements ratios of groups (2) and (3) samples. This pattern is indicative of removal by fractional crystallization of a mineral phase for which Rb, Ta and HREE are incompatible and Th and LREE compatible. Such mineral phase could be monazite. Actually, group (1) diorites lack accessory mineral such as monazite and apatite, which are always present in group (2) and (3) diorites.

In conclusion, all the analyzed samples belong to the same fractionation trend and are related with the melting of a metasomatized mantle in a supra-subduction zone context. More precisely based on Shervai's (1982) discrimination diagram the studied mafic rocks show characteristics of rocks emplaced in a back-arc environment (Fig. 8).

3.4 Geochronology, thermochrology.

In order to constrain the timing of emplacement of the MangTsa granite and of the mafic rocks, zircons from six samples were dated by the U/Pb in-situ technique with a LA-ICP-MS at the Laboratoire Magma et Volcans, Clermont-Ferrand (France). U/Pb data are reported in Table 2 and Fig. 9. The details of the analytical methods and settings are given in appendix A1. To constrain the subsequent thermal history three samples were dated with the $^{40}Ar/^{39}Ar$ at the geochronology laboratory of Geosciences Montpellier (Université de Montpellier 2, France): two slightly deformed leucocratic muscovite and biotite bearing granites (K1C20 and K1C21), and one strongly deformed granite (K1C11) (Fig. 2a). $^{40}Ar/^{39}Ar$ data are given in Tables 3, 4 and 5 and in Fig. 10. The details of the analytical methods and settings are given in appendix A2. Muscovites and biotites of an undeformed muscovite rich leucocratic granite (K89G181) were previously dated (Matte et al., 1996), A summary of the available geochronological data is given in table 6.

Twenty-two U/Pb analyses of zircon rims from K1C21 define a Discordia line intersecting the Concordia at 116.9 ± 0.1 Ma (Fig. 9b). Five sub-concordant other data produce older ages scattering between 350 Ma to 740 Ma (Fig. 9a). This underline a strong and heterogeneous inheritance, coupled to moderate Pb loss. The data suggest that granite emplacement took place in the lower Cretaceous at 117 Ma and that some parts of the zircons were inherited from a basement ~800 Ma old. The occurrence of such inherited grain further attest for a crustal origin for the leucogranite.

Zircons from the dacites and diorites yield precisely-defined lower intercept ages ranging from 116.4 ± 1.2 Ma (K1L23 and 24 diorites), to 103.9 ± 2.3 Ma (K1L25 dacite), 98.7 ± 1.4 Ma (K1L17 dacite) and 95.1 ± 1.7 Ma (K1L26 dacite) (Fig. 9, Table 2, Table 6).

$^{40}Ar/^{39}Ar$ dating of micas also yields Cretaceous ages (Fig. 10). Muscovites display plateaus ages between 100.7 (K1C11) and 103 Ma (K1C20). K1C21 biotite with age steps climbing from 88 to 95 Ma and a total fusion age of ca 95 Ma. K89G181 muscovite and biotite yields respectively plateau ages of 91.6±1.7 and 87.5±0.4 (Matte et al., 1996)

K-feldspar age spectra are complex with excess argon in the first step and similar patterns for both samples K1C20 and K1C21: a first pseudo-plateau at 60-57 Ma, then a regular increase towards ages of the coexisting micas (Fig. 10b,c). Such age spectra are typically associated with slow cooling of the feldspars. These age spectra can be modelled using volume diffusion equation (Lovera, 1992; Lovera et al., 1989). The resulting models (Fig. 11) show a rather monotonous cooling, in agreement with the mica ages, from late Cretaceous times until ca 55-60 Ma when both samples start to cool much more rapidly. At that time cooling increase by a factor of 5 to reach ca 20°C/Ma. Following this event, mean cooling rate to present time appears to be very slow, of about 2°C/Ma. However, the timing of the slowing down of the cooling cannot be constrained with our data.

4 Discussion: geological history of western Tibet

4.1 Proterozoic inheritance

Zircon from sample K1C21 show a Neo-Proterozoic inheritance, whilst very imprecise. Proterozoic ages in Tibet have already been reported, especially from the border areas such as the cratons of Tarim, Qaidam or Songpan-Garze. It appears that most cratonic areas around Tibet especially in the North, and elsewhere in Asia have recorded several Proterozoic events at least 900 Ma old (Arnaud et al., 2003; Gehrels et al., 2003; Roger et al., 2003; Sobel and Arnaud, 1999). Our data suggest that a comparably an old basement (~800 Ma) exists below west-central Tibet and especially in Qiangtang. This extends further south the existence of a very old crust upon which a large part of Tibet would rest.

4.1 Lungmu Co suture.

The LMC fault zone has been assigned a position at the boundary between the Tienshuihai terrane (lateral equivalent to the Bahay Har terrane and the evermore eastern Songpan terrane) to the north, and the Qiangtang block (Matte et al., 1996) and then would be a the lateral equivalent of the Jinsha Triassic suture zone (e.g., Matte et al., 1996). In the absence of any ultamafic rocks, the suture was considered as “cryptic”, the remnants of the suture zone being either eroded, buried or offset by later faults (e.g., Baud, 1989; Pan et al., 1992). In east Tibet, the Jinsha suture is associated with the last stage (lower Jurassic) of the so-called “Indosinian” collision between the South China, North China, Kunlun, Qiangtang and Yindung cratons (e.g., Faure et al., 1999; Lin et al., 2000; Mattauer et al., 1985, Roger et al., 2010). Roger et al. (2003) have documented the south dipping Indosinian Jinsha suture as far west as Yushu (~97°E). More to the west, Permo-Triassic ophiolitic bodies are found along strike until ~90°E (Xijir Ulan lake). According to the Chengdu institute of geology and mineral resources (2004) geological map other ophiolites are found westward along strike at ~84°E, East and West of the Yanghu Lake (Y, Fig. 1a). Our study suggest that no ultrabasic rocks outcrop in the LMC range making improbable a direct prolongation of the Jinsha suture zone towards the SW. This does not disprove, that the LMC zone is the present day boundary between the Tianshuihai terrane and the Qiangtang block but suggest that the suture is located further North and / or has been significantly offset by the Lungmu Co fault.

4.2 Cretaceous magmatism and cooling.

Our new U/Pb ages on Diorites, dacite and granite imply that a major magmatic event took place in the LMC area between 120 and 90 Ma (Middle Cretaceous). The mafic magmatism is indicative of a supra-subduction context and the granite results from crustal anatexis. So far these Cretaceous magmatic rocks are the only one known in northern Qiangtang area. More to the east, contemporaneous sub-aerial tuff and basalts have been described between Gerze and Nyima in southern Qiangtang bloc, as well as ~150 km further north (white dots on Fig. 1a) (Kapp et al., 2005). This magmatism is interpreted as being related with the final subduction of the Lhasa block beneath Qiangtang that ultimately resulted in the formation of the Nujiang suture (e.g., Kapp et al. 2005). The magmatic activity in the LMC area ~100 km north of the Nujiang suture (Fig. 1a), with diorites and dacites having back arc geochemical compositions (Fig. 8), could be due to back arc extension above that subduction.

Our mapping, as well as previous work (Matte et al., 1996), does not reveal mafic rocks nor cretaceous granite within the Tianshuihai terrane north of the LMC fault zone (Fig. 1b). This could be due to westward shift of potential outcrops by the LMC fault where no detailed field work has been performed so far. Another possibility, is that such potential magmatic rocks located on the southern egde of the Tianshuihai terrane have been underthrust below the northern Qiantang bloc in the location of what will later be the LMC strike slip fault. Actually Matte et al. (1996) recognized a post 100Ma north-south compression event in the LMC range. This event is contemporaneous with a compression event documented in southern Qiangtang following the cretaceous magmatic event (Kapp et al., 2005).

All micas $^{40}Ar/^{39}Ar$ ages of the MangTsa granite span in age between 87 and 103 Ma. Assuming closure temperatures of 390±45°C for the white micas (Hames and Bowring, 1994) and 320±40°C for the biotites (Harrison et al., 1985) a first-order cooling history of the Lungmu Co range can drawn (Fig. 11). After granite emplacement at ~117 Ma, temperature dropped below ~320°C in the Upper Cretaceous (95-90 Ma). This relatively long cooling time coincide with the timing of emplacement of the mafic rocks that span in age from ~116 to ~95 Ma (Table 6,Fig. 11). Cooling of the eastern undeformed granite (K89G181) appears to take place 7 to 10 Ma after the deformed part of the granite (K1C11, 20 & 21). This could suggest that deformation occurred prior to cooling below ~350°C, which is compatible with the textural mineral observations. In that interpretation, deformation would have occurred during late granite emplacement. However the age pattern is not confirmed by K1C20 Kf cooling history.

4.3 Cenozoic cooling: a far effect of the India-Asia collision ?

Taken altogether, thermochronologic data suggest a rather slow cooling since ~85 Ma at ~3.5°C/Ma on average. However, diffusion modelling of K-feldspar data suggest an increase of the cooling rate to ~20°C at 60-65 Ma for both MangTsa granite samples (Fig. 11). Such cooling rate is compatible with tectonically driven exhumation event that could explain the erosion of the Mesozoic cover south of the LMC fault zone, but not north of it. This differential exhumation likely did not take place during the Neogene, as Tertiary sediments outcrop at the same elevation on both sides of the LMC fault zone. This Paleocene exhumation episode may correlate with the Tertiary (Post ~60 Ma) faulting recognized by Kapp et al., (2005) in southern Qiangtang and the early Eocene continental subduction in Central Qiangtang (Roger et al., 2000).

Although age estimates for the India – Eurasia collision range between 65 and 35 Ma (see Guillot et al., 2003 for a review), most authors consider that it started between 55 and 60 Ma ago in Northwest Himalaya (e.g., Beck et al., 1995; Treloar & Coward, 1991; Guillot et al., 2008). This timing corresponds to that of the last fast cooling in the LMC range (Fig. 11) suggesting a causal link. Van der Beek et al. (2009) published (U-Th)/He ages of 17.2+/-0.6 Ma (apatite, K1L23) and 24.7+/-0.5 Ma (zircon, sample K1L24) for two diorite boulders of the LMC range. If taken into account in the cooling history, the zircon U-Th/He age could suggest a slight Tertiary reheating (path 1, Fig. 11). However, this age has to be taken with caution as it results from a single aliquot. The most likely hypothesis is that after 55 Ma, the cooling rate slowed down to less than 2°C/Ma (path 2, Fig. 11), corresponding to a small degree of exhumation until recent time. This is compatible with the interpretation of Van der Beek et al. (2009) of the formation of the north-western part of the Tibetan plateau around Paleocene/Eocene time, together with the Kohistan and Ladakh, and its preservation since then. The formation of the northwest part of the Tibetan plateau could predate that of its north-central one, as paleo-altimetric data suggest that the latter reached its present day elevation at ca. 35 Ma (Rowley & Curry, 2006; Dupont-Nivet et al., 2008), following increased exhumation rates at ~50Ma (Clark et al., 2010). This possible diachronism of Tibet uplift could hypothetically be related with an earlier onset of collision in the west followed by an eastward growth (Tapponnier et al., 2001; Yin et al., 2002). This would be compatible with studies proposing that collision occurred at 60-55 Ma in the west (Beck et al., 1995; Treloar & Coward, 1991) and around 50 Ma in central Himalaya (see Guillot et al., 2003 for review).

5. Summary of new hints on northwest Tibet geological evolution.

Our field study, geochemical and geochronological analyses in the eastern Lungmu Co (LMC) range, immediately south of the LMC lake yield some hints on the tectono-magmatic evolution of one of the highest, poorly known part of the Tibetan plateau. It provides new constraints on the geodynamic evolution of western Tibet since the upper Paleozoic, whilst many of the conclusions await more detailed confirmations and additional field-studies.

The LMC fault zone corresponds to the boundary between the QiangTang block of Gonwanian affinity to the South and the Tianshuihai terrane of Laurasian affinity to the north but do not show ultrabasic rocks that would testify for a Paleo-Tethyan subduction during the Permian. A major magmatic event occurred in the middle Cretaceous (117-95 Ma), with crustal partial melting generating the Mang Tsa leucogranite, and intrusion of mafic rocks. The geochemistry of the mafic rock indicates that they emplaced in a back arc setting probably north of and above the Nujiang subduction. We infer from field observation and thermochronological resuls that the LMC zone has been reactivated as a thrust at the onset of the India-Eurasia collision at ~60 Ma. South of the LMC fault this caused the erosion of the Mesozic cover and an exhumation of few km, probably at the time of the building of the northwesten Tibetan plateau. The LMC zone has then been affected, and possibly offset, by a en echelon series of WSW-ENE left-lateral strike-slip faults that connect with the Altyn Tagh fault, and that are associated with few N-S active normal faults.

Acknowledgements.

We are grateful to Michael Flowerdew and an anonymous reviewer for their comments. The fieldwork was financed by the French INSU Dyeti programm.

Bibliography

Armijo, R., Tapponnier, P., Mercier, J.L., Han, T., 1986. Quaternary extension in Southern Tibet: field observations and tectonic implications. Journal of Geophysical Research 91, 13803-13872.

Arnaud, N., Tapponnier, P., Roger, F., Brunel, M., Scharer, U., Wen, C., Xu, Z.Q., 2003. Evidence for Mesozoic shear along the western Kunlun and Altyn-Tagh fault, northern Tibet (China). Journal of Geophysical Research-Solid Earth 108, 2053, doi:2010.1029/2001JB000904.

Baud, A., 1989. The western end of the Tibetan plateau, In: Sengör, A.M.C. (Ed.), Tectonic evolution of the Tethyan region, Amsterdam, pp. 505-506.

Beck, R.A., Burbank, D.W., Sercombe, W.J., Riley, G.W., Barndt, J.K., Berry, J.R., Afzal, J., Khan, A.M., Jurgen, H., Metje, J., Cheema, A., Shafique, N.A., Lawrence, R.D., Khan, M.A., 1995. Stratigraphic evidence for an early collision between northwest india and asia. Nature 373, 55-58.

Beck, R.A., Burbank, W., Sercombe, W.J., Khna, A.M., Lawrence, R.D., 1996. Late Cretaceous ophiolite obduction and Paleocene India-Asia collision in the westernmost Himalaya. Geodinamica Acta 9, 114-144.

Cheng, J., Xu, G., 1986. Geologic map of the Gaize region with report. Chengdu, People's Republic of China.

Chevalier, M.L., Ryerson, F.J., Tapponnier, P., Finkel, R.C., Van Der Woerd, J., Li, H., and Qing, L., 2005, Sliprate measurements on the Karakoram fault may imply secular variations in fault motion: Science, v. 307, p. 411–414, doi: 10.1126/science.1105466.

Chengdu Institute of Geology and Mineral Resources China, Geological Survey, 2004. Geological Map of Qinghai-Xizang (Tibet) plateau and adjacent areas, In: Chengshu, W., Kedong, H. (Eds.). Chengdu Cartographic Publishing House, Chengdu.

Clark, M.K., Farley, K.A., Zheng, D., Wang, Z., Duvall, A.R., 2010. Early Cenozoic faulting of the northern Tibetan Plateau margin from apatite (U-Th)/He ages. Earth and Planetary Science Letters 296, 78.

Dupont-Nivet, G., Hoorn, C., Konert, M., 2008. Tibetan uplift prior to the Eocene-Oligocene climate transition: Evidence from pollen analysis of the Xining Basin. Geology 36, 987-990.

Dupont-Nivet, G., Horton, B.K., Butler, R.F., Wang, J., Zhou, J., Waanders, G.L., 2004. Paleogene clockwise tectonic rotation of the Xining-Lanzhou region, northeastern Tibetan Plateau. Journal of Geophysical Research-Solid Earth 109, doi:10.1029/2003JB002620.

Evensen, N.M., Hamilton, P.J., O'Nions, R.K., 1977. Rare earth abundances in chondritic meteorites. Geochimica et Cosmochimica Acta 42, 1199-1212.

Faure, M., Lin, W., Shu, L., Sun, Y., Sharer, U., 1999. Tectonics of the Dabieshan (eastern China) and possible exhumation mechanism of ultra high-pressure rocks. Terra Nova 11, 251-258.

Guillot, S., Garzanti, E., Baratoux, D., Marquer, D., Maheo, G., de Sigoyer, J., 2003. Reconstructing the total shortening history of the NW Himalaya. Geochemistry Geophysics Geosystems 4, 1064, doi:1010.1029/2002GC000484.

Guillot, S., Maheo, G., de Sigoyer, J., Hattori, K.H., Pecher, A., 2008. Tethyan and Indian subduction viewed from the Himalayan high- to ultrahigh-pressure metamorphic rocks. Tectonophysics 451, 225-241.

Hames, W. E., and S. Bowring (1994), An empirical evaluation of the argon diffusion geometry in muscovite, *Earth & Planetary Science Letter*, *124*, 161-169.

Harrison, T. M., et al. (1985), Diffusion of 40Ar in biotite: Temperature, pressure and compositional effect, *Geochim. Cosmochim. Acta*, *49*, 2461-2468.

Harrison, T.M., Copeland, P., Kidd, W.S.F., Yin, A., 1992. Raising Tibet. Science 255, 1663-1670.

Hilairet, N., 2002. Pétrographie et thermobarométrie sur des métapélites à grenat-staurotide du Nord-Ouest Tibet (Qiangtang). Unpublished master report. Université Lyon 1.

Jolivet, M., Brunel, M., Seward, D., Xu, Z., Yang, J., Malavieille, J., Roger, F., Leyreloup, A., Arnaud, N., Wu, C., 2003. Neogene extension and volcanism in the Kunlun Fault Zone, northern Tibet: New constraints on the age of the Kunlun Fault. Tectonics 22, doi: 10.1029/2002TC001428.

Kapp, P., DeCelles, P.G., Gehrels, G.E., Heizier, M., Ding, L., 2007. Geological records of the Lhasa-Qiangtang and Indo-Asian collisions in the Nima area of central Tibet. Geological Society of America Bulletin 119, 917-932.

Kapp, P., Yin, A., Harrison, T.M., Ding, L., 2005. Cretaceous-Tertiary shortening, basin development, and volcanism in central Tibet. Geological Society of America Bulletin 117, 865-878.

Kapp, P., Yin, A., Manning, C.E., Harrison, T.M., Taylor, M.H., Ding, L., 2003. Tectonic evolution of the early Mesozoic blueschist-bearing Qiangtang metamorphic belt, central Tibet. Tectonics 22, 1043, doi:1010.1029/2002TC001383.

Leloup, P. H., et al., 2011, Long-lasting intracontinental strike-slip faulting: new evidence from the Karakorum shear zone in the Himalayas, *Terra Nova*, *23*, 92-99.

Lin, W., Faure, M., Monie, P., Scharer, U., Zhang, L.S., Sun, Y., 2000. Tectonics of SE China: New insights from the Lushan massif (Jiangxi Province). Tectonics 19, 852-871.

Liu, Q., Avouac, J.P., Tapponnier, P., Zhang, G.W., 1991. Holocene and active faulting in western Qantang. Terra Nova Abstr. 3, 265.

Lovera, O.M., 1992. Computer-Programs to Model Ar-40/Ar-39 Diffusion Data from Multidomain Samples. Computers & Geosciences 18, 789-813.

Lovera, O.M., Richter, F.M., Harrison, T.M., 1989. 40Ar/39Ar geothermometry for slowly cooled samples having a distribution of diffusion domaine size. 94, 917-936.

Mattauer, M., Matte, P., Malavieille, J., Tapponnier, P., Maluski, H., Xu, Z.Q., Lu, Y.L., Tang, Y.Q., 1985. Tectonics of the Qinling Belt - Buildup and Evolution of Eastern Asia. Nature 317, 496-500.

Matte, P., Tapponnier, P., Arnaud, N., Bourjot, L., Avouac, J.P., Vidal, P., Liu, Q., Pan, Y., Wang, Y., 1996. Tectonics of Western Tibet, between the Tarim and the Indus. Earth and Planetary Science Letters 142, 311-316.

Molnar, P., Tapponnier, P., 1977. Active tectonics of Tibet. Journal of Geophysical Research 83, 5361-5375.

Norin, E., 1946. Geological exploration in western Tibet. Rep. from the Swedish exp. to the NW prov. China under the leadership of dr. SVEN HEDIN. Geology III, 7.

Pan, Y., Zheng, D., Zhang, Q., 1992. Introduction to integrated scientific investigation on Karakorum and Kunlun mountains. China Meterological Press, Beijing.

Paquette, J.L., Montel, J.M., Chopin, C., 1999. U-Th-Pb dating of the Brossasco ultrahigh-pressure metagranite, Dora-Maira massif, western Alps. European Journal of Mineralogy 11, 69-77.

Passchier, C.W., Trouw, R.A.J., 1996. Microtectonics. 289pp., Springer, Berlin.

Peltzer, G., Saucier, F., 1996. Present-day kinematics of Asia derived from geologic fault rates. Journal of Geophysical Research-Solid Earth 101, 27943-27956.

Raterman, N.S., Cowgill, E., Lin, D., 2007. Variable structural style along the Karakoram fault explained using triple-junction analysis of intersecting faults. Geosphere 3, 71-85.

Robinson, D.M., Dupont-Nivet, G., Gehrels, G.E., Zhang, Y.Q., 2003. The Tula uplift, northwestern China: Evidence for regional tectonism of the northern Tibetan Plateau during late Mesozoic-early Cenozoic time. Geological Society of America Bulletin 115, 35-47.

Robinson , A. C., 2009. Evidence against Quaternary slip on the northern Karakorum Fault suggests kinematic reorganization at the western end of the Himalayan–Tibetan orogen. E.P.S.L. 286, 158-170.

Roger, F., Arnaud, N., Gilder, S., Tapponnier, P., Jolivet, M., Brunel, M., Malavieille, J., Xu, Z.Q., Yang, J.S., 2003. Geochronological and geochemical constraints on Mesozoic suturing in east central Tibet. Tectonics 22, 1037, doi:1010.1029/2002TC001466.

Roger, F., Jolivet, M., Malavieille, J., 2010. The tectonic evolution of the Songpan-Garze (North Tibet) and adjacent areas from Proterozoic to Present: A synthesis. Journal of Asian Earth Sciences 39, 254-269.

Roger, F., Tapponnier, P., Arnaud, N., Schärer, U., Brunel, M., Xu, Z.Q., Yang, J.S., 2000. An Eocene magmatic belt across central Tibet: mantle subduction triggered by the Indian collision? Terra Nova 12, 102-108.

Rowley, D.B., Currie, B.S., 2006. Palaeo-altimetry of the late Eocene to Miocene Lunpola basin, central Tibet. Nature 439, 677-681.

Sengör, A.M.C., Okurogullari, A.H., 1991. The role of accretionnary wedges in the growth of continents: Asiatic exemple from Argand to plate tectonics. Eclogae Geologicae Helveticae 84, 535-597.

Shervai, J.W., 1982. Ti-V plots, the petrogenesis of modern, ophiolitic lavas. Earth and Planetary Science Letters 59, 101-118.

Sobel, E.R., Arnaud, N., 1999. A possible middle Paleozoic suture in the Altyn Tagh, NW China. Tectonics 18, 64-74.

Stesky, R.M., 1978. Mechanisms of High-Temperature Frictional Sliding in Westerly Granite. Canadian Journal of Earth Sciences 15, 361-375.

Sun, S.S., McDonough, W.F., 1989. Chemical and isotopics sytematics of oceanic basalts: implication for mantle composition and processes. In: Magmatism in ocean basins, Saunders A.D. and Norry M.J. (eds.). Geological Society of London Special Publication 42, 313-345.

Tapponnier, P., Zhiqin, X., Roger, F., Meyer, B., Arnaud, N., Wittlinger, G., Jingsui, Y., 2001. Oblique Stepwise Rise and Growth of the Tibet Plateau. Science 294, 1671-1677.

Tapponnier, P. and Molnar P., 1977. Active faulting and tectonics in China. J.G.R., vol. 82, 20, 2905-2930.

Tatsumi, Y., Hamilton, D.L., Nesbitt, R.W., 1986. Chemical characteristics of fluid phase released from a subducted lithosphere and origin of arc magmas: evidence from high-pressure experiments and natural rocks. J. Volcano. Geotherm. Res. 29, 293-309.

Treolar, P.J., Coward, M.P., 1991. Indian plate motion and shape: constraints on the geometry of the Himalaya orogen. 191, 189-198.

Valli, F., Leloup, P.H., Paquette, J.-L., Arnaud, N., Li, H., Tapponnier, P., Lacassin, R., Guillot, S., Liu, D., Deloule, E., Xu, Z., Mahéo, G., 2008. New U/Pb constraints on timing of shearing and long-term slip-rate on the Karakorum fault. Tectonics 27. doi:10.1029/2007TC002184.

Van der Beek, P., Van Melle, J., Guillot, S., Pecher, A., Reiners, P.W., Nicolescu, S., Latif, M., 2009. Eocene Tibetan plateau remnants preserved in the northwest Himalaya. Nature Geoscience 2, 364-368.

Wallis, S., Tsujimori, T., Aoya, M., Kawakami, T., Terada, K., Suzuki, K., Hyodo, H., 2003. Cenozoic and Mesozoic metamorphism in the Longmenshan orogen: Implications for geodynamic models of eastern Tibet. Geology 31, 745-748.

Yin, A., Rumelhart, P.E., Butler, R., Cowgill, E., Harrison, T.M., Foster, D.A., Ingersoll, R.V., Zhang, Q., Zhou, X.Q., Wang, X.F., Hanson, A., Raza, A., 2002. Tectonic history of the Altyn Tagh fault system in northern Tibet inferred from Cenozoic sedimentation. Geological Society of America Bulletin 114, 1257-1295.

Tables captions

Table 1: Whole rock analysis of mafic rocks

Table 2: U/Pb data

Table 3: Micas $^{40}Ar/^{39}Ar$ data.

Table 4: K1C20 Kf $^{40}Ar/^{39}Ar$ data.

Table 5: K1C21 Kf $^{40}Ar/^{39}Ar$ data.

Table 6: Geochronological data summary

Appendix captions

Appendix A 1: LA-ICPMS instrumentation and analytical method.

Appendix A 2: Ar/Ar instrumentation and analytical method.

Figure captions

Figure 1: Geological frame of NW Tibet. **(a)** Main active faults and major paleogeographic blocks of Tibet superimposed on SRTM DEM. BC: Bangong Co, LMCF: Lungmu Co fault, GF: Gozha fault, G: Gerze, L: Lungmu Co range, N: Nyima, Y: Yanghu, XU: Xijir Ulan. North Kunlun suture : Early Paleozoic, South Kunlun and Jinsha sutures: late Paleozoic – early Mesozoic, Nujiang suture: middle Mesozoic, Yarlung-Zangpo: Tertiary. Frame corresponds to the studied area (Fig. 1b). White points indicate Cretaceous mafic volcanism (Kapp et al., 2005); **(b)** Schematic structural map of North-western Tibet Plateau. From Matte et al., (1996), Chengdu geological institute, (2004), modified from Landsat ETM+ image interpretation. Inset shows the location of Fig. 2a.

Figure 2: **(a)** Structural map of the central Lungmu Co range. Map drawn from SPOT and Landsat ETM+ image interpretation and field observations. **(b)** Geological cross sections across the LMC range. Sections are located on Fig. 2a.

Figure 3: field observations. **(a)** View of the northern edge of the Lungmu Co (LMC) range. Point of view shown on Fig. 2a. **(b)** Verticalized (Eocene?) red beds in the LMC fault zone (section A, Fig. 2a). **(c)** Steep E-W micaschist with horizontal stretching lineation in the LMC fault zone. Hammer gives scale (section A, Fig. 2a). **(d)** C/S structures in calcschists of the LMC fault zone (section A, Fig. 2a). View from above. Lens gives scale. **(e)** trace of the active LMC fault in quaternary sediments southwest of the Sum Xi Co. The two arrows labelled F show the fault trace while the two labelled T show an ~90 m offset of a strath terrace. Google earth image 34°29’30”N, 80° 04’E.

Figure 4: Plots of selected major elements versus MgO for the Lungmu Co mafic rocks. Group (1): ◊, Group (2): □; Group (3): Δ.

Figure 5: Chondrite-normalized REE and MORB-normalized multi-element plots for the Lungmu Co mafic rocks. Chondrite and MORB normalization values from Evensen et al. (1977) and Sun and McDonough (1989), respectively. Same symbols as in Fig. 4.

Figure 6: Plot of mobile (Sr) versus immobile (Pr, Nd) elements. This diagram discriminate the effects of fractional crystallization and remobilization of LILE elements by fluids. Same symbols as in Fig. 4.

Figure 7: Plots of incompatible elements ratios versus transition elements. Same symbols as in Fig. 4.

Figure 8: Ti vs V discrimination diagram of Shervai (1982). IAT: Island rc Tholeiites, MORB: Mid Oceanic Ridge Basalts, BABB: Back-Arc Basin Basalt, OIB: Oceanic Island Basalt. Same symbols as in Fig. 4.

Figure 9: U/Pb data. **a & b)** K1C21, **c)** K1L17a,b; **d)** K1L23 and 24 **e)** K1L25; **f)** K1L26;. All data-point error ellipses are 2σ. See data in Table 2 abd Table 6.

Figure 10: Ar/Ar data **a)** $^{40}Ar/^{39}Ar$ results for muscovites and biotites. All ages are at 1σ including the error on J factor. Muscovite ages are plateaus Biotite age is a total fusion (TF) age. **b)** K1C20 Kf, **c)** K1C21 Kf. For b and c, age spectrum (black) of each sample is shown together with the one calculated for the best cooling history shown in Fig. 11 (thick grey line).

Figure 11: Thermal history of the Lungmu Co range. K1C20 & 21 K-feldspar cooling patterns modelled assuming a multi-domain diffusion process developed by Lovera and co-workers (see references in the text). Modelling has tested various solutions by a Monte Carlo algorithm to assess the variance of the resulting best fits. Grey shaded area, are the distribution at 90% confidence intervals of the best-fit cooling histories. Inner black and open diamond lines are the median 90% confidence intervals of the best fit cooling history. Closure temperature for other thermochronological systems as given in text. Note that the volcanic rocks probably intruded in country rocks cooler than the closure temperature. (U-Th)/He data from Van der Beek et al., (2009). Ages ranges reported for the India-Asia onset of collision and for timing of deformation in northern Tibet are shown for comparison. Two possible cooling paths are shown.

Tables

Table 1: Whole rock analyses of basic rocks.

Sample	KIL 28b	KIL 29	KIL 30	KIL 48	KIL 16	KIL 17	KIL 21	KIL 22	KIL 23	KIL 24	KIL 25b	KIL 26	KIL 27	KIL 46	KIL 47	KIL 24b
Type	Amphibolite	Diorite	Diorite	Amphibolite	Dacite	Dacite	Amphibolite	Diorite	Diorite	Diorite	Dacite	Dacite	Basalt	Amphibolite	Amphibolite	Diorite
Group	1	1	1	1	2	2	2	2	2	2	2	2	2	2	3	3
SiO_2	49.56	49.96	47.92	50.84	60.94	62.51	51.42	46.88	44.87	44.39	66.6	62.15	44.23	47.79	42.35	55.16
TiO_2	1.1	0.93	1.16	1.19	0.68	0.68	1.14	1.65	1.13	1.73	0.55	0.67	1.67	4.23	2.34	1.18
Al_2O	13.59	14.79	13.32	14.68	15.09	15.6	10.82	11.54	19.85	17.14	16.09	15.06	14.83	12.92	9.05	16.47
Fe_2O_3	14.01	13.28	14.08	9.79	4.06	5.45	9.5	11.52	10.19	11.35	4.37	6.14	12	15.79	10.7	6.54
MnO	0.22	0.23	0.19	0.18	0.17	0.09	0.14	0.17	0.12	0.12	0.09	0.1	0.17	0.22	0.16	0.1
MgO	6.56	6.94	6.92	7.78	1.83	2.34	11.98	11.79	6.15	8.01	1.2	3.04	11.2	5.59	12.74	4.75
CaO	8.58	9.69	7.08	10.33	6.55	4.37	9.28	10.19	9.75	10.46	3.34	3.94	10.8	8.36	15.06	7.16
Na_2O	2.36	1.88	2.22	2.71	3.71	2.49	1.79	2.27	2.47	2.13	2.62	2.73	1.66	2.73	1.31	2.8
K_2O	0.51	1.31	0.48	1.27	2.48	2.84	0.74	0.67	1.76	1.27	3.99	2.92	1.19	0.47	0.7	2.23
P_2O_5	0.1	0.08	0.09	0.11	0.17	0.16	0.37	0.35	0.62	0.88	0.16	0.16	0.45	0.57	1.32	0.95
LOI	3.41	1.36	5.9	0.84	4.18	2.32	1.97	2.07	2.11	2.11	1.44	2.09	1.9	0.8	3.49	2.13
H_2O-	0.12	0.13	0.22	0.13	0.18	0.27	0.2	0.11	0.12	0.08	0.2	0.17	0.09	0.11	0.14	0.12
Ba	412.9	708.6	604.5	50.6	777.8	642.3	527.1	339.1	700.5	742.5	1025.9	812.2	511.8	140.4	2072.0	2132.2
Rb	20.8	46.6	19.8	123.8	57.4	85.4	14.2	14.5	59.5	33.2	161.1	87.3	30.6	13.4	21.3	62.8
Sr	336.8	562.3	340.9	101.1	292.6	340.8	478.9	887.5	1409.9	1218.3	352.5	413.0	632.4	378.2	922.3	1557.0
Ta	0.5	0.5	0.4	0.7	1.4	1.2	0.7	1.0	0.5	0.6	1.3	1.1	0.9	2.0	3.0	0.9
Th	0.8	0.4	0.4	0.3	16.5	15.3	10.4	10.2	5.6	8.6	15.4	14.1	3.7	3.5	11.0	37.1
Zr	54.5	37.3	49.8	11.9	117.7	59.4	61.9	63.6	33.5	41.8	108.1	76.5	56.1	128.8	307.2	59.1
Nb	6.2	4.7	4.2	3.4	15.0	14.8	11.9	14.9	8.3	9.8	16.8	15.3	11.4	30.4	70.9	18.4
Y	23.1	17.8	19.7	19.3	20.7	19.5	17.3	29.1	16.6	25.4	22.3	19.7	28.6	28.3	19.0	25.8
Hf	1.7	1.1	1.4	0.6	3.3	2.0	2.2	2.6	1.4	1.6	3.2	2.5	2.3	3.0	7.1	1.5
V	335.9	321.9	346	270.8	77.4	103.6	222.2	323.8	227.2	387.3	76.6	99.8	347.3	426.9	224.3	214.4
Cr	32.1	70.9	56.6	256.7	21.8	29.5	570.3	372.4	81	121.3	31.8	28.2	401.5	90.6	418.7	58.6
Ni	54.9	71.9	61.1	87.4	6.2	8	126.2	97.6	28.5	39.1	4.5	7.8	84.7	83.3	234.7	20.1
Co	50.2	54.3	53.4	38.4	8.7	10.3	45.1	50.1	29.6	40.8	6.9	12.1	42.7	47.5	44.8	20.5
U	0.19	0.17	0.12	1.62	3.20	2.21	1.40	1.46	0.81	1.30	3.22	3.21	0.49	0.94	2.56	3.46
Sc	45.1	51.5	44.4	38.8	12.4	14.7	37.6	51.3	24.9	45.5	10.7	12.6	46.7	32.9	26.7	25.1
Cu	138.7	89.3	192.4	16.1	4.3	10	50.8	34.6	43	27.5	4.6	12.9	58.9	76.6	30.5	9.7
Zn	129.5	75.2	177.7	9.5	5.6	10.6	56.2	38.9	44.5	29.2	4.0	13.3	48.5	65.2	23.9	11.1
Pb	5.8	5.7	5.2	11.0	38.8	50.9	8.9	3.8	8.1	8.5	69.6	44.2	3.9	20.8	681.4	19.3
La	6.0	4.4	4.6	2.1	35.0	43.7	68.8	83.2	65.9	89.0	65.0	53.4	67.2	37.6	135.7	178.7
Ce	12.5	9.2	9.9	6.6	69.1	84.0	102.0	141.5	101.9	145.4	124.1	98.4	111.6	86.3	249.0	292.4
Pr	1.5	1.2	1.3	1.0	7.6	8.6	8.8	13.5	9.2	14.0	12.1	9.8	11.0	10.5	23.5	25.9
Nd	7.0	5.5	6.3	5.6	28.2	30.8	29.4	48.0	31.9	49.4	40.7	34.7	40.4	43.1	77.9	84.9
Sm	2.3	1.8	2.1	1.9	5.5	5.4	4.8	7.9	5.2	8.4	6.9	5.9	6.8	8.9	10.2	12.1
Eu	0.8	0.6	0.6	0.7	1.1	1.1	1.2	2.0	1.4	2.1	1.3	1.2	1.8	3.0	2.8	2.8
Gd	3.2	2.5	2.9	2.7	3.7	3.5	3.1	5.1	3.4	5.2	3.8	3.4	4.8	6.7	3.1	4.6
Tb	0.6	0.4	0.5	0.5	0.7	0.6	0.6	0.9	0.6	0.9	0.7	0.6	0.9	1.1	0.7	0.9
Dy	3.9	3.0	3.5	3.2	3.9	3.7	3.4	5.4	3.4	5.5	4.1	3.7	5.4	5.8	3.8	5.1
Ho	0.9	0.7	0.8	0.7	0.7	0.7	0.7	1.1	0.6	1.0	0.8	0.7	1.0	1.0	0.7	0.9
Er	2.8	2.0	2.4	2.2	2.2	2.0	2.0	3.3	1.9	2.8	2.5	2.2	3.0	2.9	1.9	2.6
Yb	2.8	2.1	2.2	2.2	2.2	2.1	1.9	3.0	1.8	2.5	2.3	2.2	2.8	2.4	2.1	2.9
Lu	0.4	0.3	0.3	0.3	0.3	0.3	0.2	0.4	0.2	0.3	0.3	0.3	0.4	0.3	0.2	0.3

K1C21 Analysis	Pb ppm	Th ppm	U ppm	Th/U	$^{2067}Pb/^{235}U$	2 σ error $^{207}Pb/^{235}U$	$^{206}Pb/^{238}U$	2 σ error $^{206}Pb/^{238}U$	Rho	Age (Ma) $^{206}Pb/^{238}U$	2 σ error $^{206}Pb/^{238}U$
06280311a	10	164	138	1,19	0,4426	0,0203	0,0557	0,0014	0,55	349,2	8,5
08280311a	112	491	1005	0,49	1,0094	0,0243	0,1033	0,0024	0,95	634	14
12280311a	31	367	1700	0,22	0,1323	0,0034	0,0181	0,0004	0,90	115,7	2,6
15280311a	16	161	724	0,22	0,1764	0,0058	0,0229	0,0005	0,70	145,7	3,3
16280311a	12	115	615	0,19	0,1390	0,0041	0,0189	0,0004	0,79	120,6	2,7
17280311a	78	549	909	0,60	0,5996	0,0141	0,0764	0,0017	0,95	474	10
18280311a	29	147	1251	0,12	0,1701	0,0048	0,0239	0,0005	0,80	152,2	3,4
19280311a	4	42	198	0,21	0,1660	0,0079	0,0216	0,0005	0,50	137,8	3,3
21280311a	10	126	493	0,25	0,1400	0,0042	0,0202	0,0005	0,75	128,6	2,9
22280311a	24	69	198	0,35	1,1228	0,0321	0,1210	0,0027	0,79	736	16
25280311a	26	278	1278	0,22	0,1488	0,0037	0,0206	0,0005	0,89	131,5	2,9
26280311a	16	180	870	0,21	0,1342	0,0036	0,0186	0,0004	0,81	118,6	2,6
28280311a	21	236	1169	0,20	0,1221	0,0031	0,0180	0,0004	0,86	115,1	2,5
29280311a	14	38	654	0,06	0,2757	0,0072	0,0190	0,0004	0,84	121,3	2,7
30280311a	29	472	1495	0,32	0,1297	0,0031	0,0191	0,0004	0,93	121,9	2,6
31280311a	20	142	1064	0,13	0,1690	0,0047	0,0191	0,0004	0,79	121,6	2,6
35280311a	46	637	1909	0,33	0,3247	0,0073	0,0193	0,0004	0,97	123,1	2,6
36280311a	34	537	1830	0,29	0,1392	0,0033	0,0182	0,0004	0,89	116,4	2,5
37280311a	44	700	2394	0,29	0,1230	0,0029	0,0183	0,0004	0,89	116,7	2,4
38280311a	18	147	816	0,18	0,2649	0,0065	0,0195	0,0004	0,87	124,4	2,6
39280311a	22	363	1231	0,29	0,1224	0,0031	0,0181	0,0004	0,83	115,4	2,4
40280311a	15	192	861	0,22	0,1233	0,0032	0,0182	0,0004	0,80	116,0	2,4
41280311a	16	199	921	0,22	0,1218	0,0032	0,0180	0,0004	0,80	115,1	2,4
45280311a	33	391	1827	0,21	0,1259	0,0029	0,0184	0,0004	0,89	117,7	2,4
46280311a	25	307	1409	0,22	0,1235	0,0033	0,0181	0,0004	0,78	115,3	2,4
47280311a	14	257	764	0,34	0,1231	0,0036	0,0181	0,0004	0,72	115,7	2,4
48280311a	28	332	1559	0,21	0,1239	0,0037	0,0180	0,0004	0,71	114,7	2,4
49280311a	15	144	857	0,17	0,1318	0,0037	0,0185	0,0004	0,73	118,2	2,4
50280311a	28	829	1393	0,59	0,1263	0,0031	0,0184	0,0004	0,84	117,3	2,4
52280311a	15	212	150	1,42	0,6144	0,0216	0,0748	0,0016	0,61	465	10
55280311a	18	234	987	0,24	0,1223	0,0030	0,0183	0,0004	0,85	116,6	2,4
56280311a	10	114	538	0,21	0,1232	0,0033	0,0182	0,0004	0,77	116,0	2,4
57280311a	19	380	997	0,38	0,1295	0,0034	0,0186	0,0004	0,78	118,8	2,4
59280311a	12	96	563	0,17	0,1561	0,0047	0,0210	0,0004	0,69	133,7	2,7

K1L17 Analysis	Pb ppm	Th ppm	U ppm	Th/U	$^{2067}Pb/^{235}U$	2 σ error $^{207}Pb/^{235}U$	$^{206}Pb/^{238}U$	2 σ error $^{206}Pb/^{238}U$	Rho	Age (Ma) $^{206}Pb/^{238}U$	2 σ error $^{206}Pb/^{238}U$
06200411e	8	212	402	0,53	0,2795	0,0096	0,0162	0,0004	0,72	103,4	2,5
07200411e	4	63	139	0,45	0,5279	0,0268	0,0170	0,0005	0,63	108,8	3,4
08200411e	11	600	603	0,99	0,1001	0,0038	0,0152	0,0004	0,63	97,5	2,3
11200411e	5	161	302	0,53	0,1013	0,0044	0,0150	0,0004	0,55	96,1	2,3
12200411e	4	110	207	0,53	0,1194	0,0060	0,0156	0,0004	0,51	99,6	2,5
15200411e	5	143	300	0,48	0,1092	0,0047	0,0159	0,0004	0,58	101,8	2,5
16200411e	6	205	273	0,75	0,2979	0,0101	0,0163	0,0004	0,73	103,9	2,6
17200411e	48	214	616	0,35	0,7070	0,0199	0,0724	0,0017	0,85	451	10
19200411e	5	169	261	0,65	0,1091	0,0045	0,0156	0,0004	0,58	99,8	2,5
21200411e	8	222	420	0,53	0,1877	0,0060	0,0156	0,0004	0,76	99,8	2,4
22200411e	5	155	315	0,49	0,1053	0,0043	0,0155	0,0004	0,60	98,8	2,4

K1L23b Analysis	Pb ppm	Th ppm	U ppm	Th/U	$^{2067}Pb/^{235}U$	2 σ error $^{207}Pb/^{235}U$	$^{206}Pb/^{238}U$	2 σ error $^{206}Pb/^{238}U$	Rho	Age (Ma) $^{206}Pb/^{238}U$	2 σ error $^{206}Pb/^{238}U$
35210411a	35	1391	1691	0,82	0,12811	0,00334	0,01818	0,00042	0,89	116,1	2,7

K1L24b Analysis	Pb ppm	Th ppm	U ppm	Th/U	$^{2067}Pb/^{235}U$	2 σ error $^{207}Pb/^{235}U$	$^{206}Pb/^{238}U$	2 σ error $^{206}Pb/^{238}U$	Rho	Age (Ma) $^{206}Pb/^{238}U$	2 σ error $^{206}Pb/^{238}U$
07210411a	8	484	274	1,77	0,1848	0,0054	0,0194	0,0004	0,77	124,1	2,8
08210411a	23	1312	912	1,44	0,1224	0,0032	0,0182	0,0004	0,89	116,4	2,6
10210411a	12	755	423	1,78	0,1418	0,0041	0,0182	0,0004	0,80	116,3	2,6
11210411a	22	1654	822	2,01	0,1244	0,0034	0,0180	0,0004	0,82	114,9	2,6
16210411a	14	1169	498	2,35	0,1521	0,0060	0,0191	0,0005	0,61	122,2	2,9
17210411a	23	1858	910	2,04	0,1272	0,0034	0,0180	0,0004	0,87	114,9	2,6
18210411a	31	2894	924	3,13	0,1225	0,0033	0,0184	0,0004	0,85	117,7	2,7
19210411a	28	1844	1063	1,73	0,1239	0,0033	0,0185	0,0004	0,86	118,4	2,7
20210411a	36	2276	1500	1,52	0,1179	0,0036	0,0177	0,0004	0,77	113,1	2,6
21210411a	37	1929	1641	1,18	0,1311	0,0033	0,0180	0,0004	0,92	114,8	2,6
22210411a	14	579	671	0,86	0,1259	0,0036	0,0182	0,0004	0,81	116,2	2,7
25210411a	20	896	859	1,04	0,1405	0,0040	0,0186	0,0004	0,84	118,7	2,7
26210411a	28	1882	1045	1,80	0,1287	0,0038	0,0182	0,0004	0,77	116,5	2,7
27210411a	28	1942	1030	1,89	0,1219	0,0035	0,0182	0,0004	0,81	116,2	2,7
28210411a	11	677	413	1,64	0,1190	0,0039	0,0184	0,0004	0,73	117,3	2,7
29210411a	14	1052	473	2,22	0,1293	0,0043	0,0187	0,0004	0,70	119,5	2,8
30210411a	12	810	441	1,84	0,1285	0,0041	0,0187	0,0004	0,74	119,4	2,8
31210411a	13	851	452	1,88	0,1290	0,0040	0,0187	0,0004	0,77	119,5	2,8
32210411a	10	754	376	2,01	0,1325	0,0049	0,0185	0,0004	0,64	118,0	2,8

K1L25 Analysis	Pb ppm	Th ppm	U ppm	Th/U	$^{2067}Pb/^{235}U$	2 σ error $^{207}Pb/^{235}U$	$^{206}Pb/^{238}U$	2 σ error $^{206}Pb/^{238}U$	Rho	Age (Ma) $^{206}Pb/^{238}U$	2 σ error $^{206}Pb/^{238}U$
38210411a	4	117	236	0,50	0,1112	0,0038	0,0160	0,0004	0,69	102,3	2,4
39210411a	4	109	205	0,53	0,1314	0,0067	0,0160	0,0004	0,51	102,6	2,6
41210411a	3	91	177	0,52	0,1094	0,0051	0,0158	0,0004	0,55	101,1	2,5
05210411b	4	96	163	0,59	0,3546	0,0120	0,0191	0,0004	0,68	121,8	2,8
06210411b	3	72	151	0,48	0,1251	0,0048	0,0164	0,0004	0,57	104,9	2,3
07210411b	11	224	658	0,34	0,1122	0,0029	0,0166	0,0003	0,78	105,8	2,2
08210411b	18	826	951	0,87	0,1176	0,0030	0,0167	0,0004	0,86	106,8	2,2
09210411b	19	750	1000	0,75	0,1169	0,0029	0,0166	0,0004	0,87	106,2	2,2

K1L26 Analysis	Pb ppm	Th ppm	U ppm	Th/U	$^{2067}Pb/^{235}U$	2 σ error $^{207}Pb/^{235}U$	$^{206}Pb/^{238}U$	2 σ error $^{206}Pb/^{238}U$	Rho	Age (Ma) $^{206}Pb/^{238}U$	2 σ error $^{206}Pb/^{238}U$
10210411b	4	118	261	0,45	0,1299	0,0045	0,0150	0,0003	0,65	95,8	2,1
11210411b	9	295	573	0,51	0,1070	0,0033	0,0152	0,0003	0,69	97,0	2,1
12210411b	6	174	360	0,48	0,0997	0,0033	0,0150	0,0003	0,65	95,8	2,1
17210411b	4	155	212	0,73	0,1153	0,0049	0,0152	0,0003	0,53	97,4	2,2
18210411b	3	138	196	0,70	0,1283	0,0057	0,0150	0,0004	0,54	95,9	2,2
19210411b	17	131	1190	0,11	0,1033	0,0027	0,0152	0,0003	0,81	97,3	2,1
20210411b	12	333	759	0,44	0,0951	0,0028	0,0143	0,0003	0,76	91,6	2,0
25210411b	23	842	1360	0,62	0,1154	0,0031	0,0145	0,0003	0,83	92,7	2,0
26210411b	13	407	605	0,67	0,3151	0,0083	0,0152	0,0003	0,85	97,1	2,2
27210411b	2	62	144	0,43	0,1029	0,0050	0,0149	0,0004	0,49	95,1	2,3
28210411b	3	107	215	0,50	0,1075	0,0045	0,0144	0,0003	0,56	92,2	2,2

Table1

Temperature °C	$^{40}Ar/^{39}Ar$	$^{38}Ar/^{39}Ar$	$^{37}Ar/^{39}Ar$	$^{36}Ar/^{39}Ar$ (10^{-3})	^{39}Ar (10^{-4} moles)	F ^{39}Ar released	%$^{40}Ar^*$	$^{40}Ar^*/^{39}Ar$	Age Ma	± 1σ Ma
K1C20Mus		Muscovite		J= 0.00431						
682	13,825	0,014	0,019	4,006	3,79	11,32	91,44	12,64	95,72	0,68
788	13,914	0,012	0,004	1,078	12,86	49,77	97,71	13,60	102,73	0,91
888	13,919	0,013	0,010	0,745	5,62	66,60	98,42	13,70	103,49	0,97
996	13,756	0,012	0,011	0,336	8,31	91,45	99,28	13,66	103,19	0,58
1220	13,729	0,012	0,341	0,538	1,96	97,30	98,99	13,59	102,72	0,95
1438	14,353	0,013	0,912	2,561	0,90	100,00	95,11	13,66	103,22	0,78

Temperature °C	$^{40}Ar/^{39}Ar$	$^{38}Ar/^{39}Ar$	$^{37}Ar/^{39}Ar$	$^{36}Ar/^{39}Ar$ (10^{-3})	^{39}Ar (10^{-4} moles)	F ^{39}Ar released	%$^{40}Ar^*$	$^{40}Ar^*/^{39}Ar$	Age Ma	± 1σ Ma
K1C11MUS		Muscovite		J= 0.00431						
687	13,297	0,013	0,046	1,756	4,27	17,09	96,12	12,78	96,74	0,55
787	13,461	0,012	0,011	0,367	9,57	55,36	99,20	13,35	100,95	0,50
891	13,629	0,012	0,028	0,339	4,63	73,89	99,28	13,53	102,26	0,84
998	13,528	0,012	0,050	0,285	4,76	92,95	99,40	13,45	101,65	0,79
1227	13,788	0,013	1,351	1,825	1,35	98,34	96,68	13,34	100,89	1,04
1434	16,243	0,019	7,187	11,183	0,42	100,00	82,34	13,45	101,66	1,25

Temperature °C	$^{40}Ar/^{39}Ar$	$^{38}Ar/^{39}Ar$	$^{37}Ar/^{39}Ar$	$^{36}Ar/^{39}Ar$ (10^{-3})	^{39}Ar (10^{-4} moles)	F ^{39}Ar released	%$^{40}Ar^*$	$^{40}Ar^*/^{39}Ar$	Age Ma	± 1σ Ma
K1C21bio		Biotite		J= 0.00431						
684	12,681	0,021	0,014	0,994	16,41	43,70	97,69	12,39	93,84	0,65
788	12,802	0,020	0,016	0,372	4,59	55,92	99,15	12,69	96,09	0,77
894	12,666	0,020	0,008	0,279	10,41	83,65	99,35	12,58	95,29	0,88
1002	12,950	0,021	0,046	0,166	5,54	98,39	99,64	12,90	97,65	0,89
1232	13,092	0,023	0,639	1,596	0,52	99,77	96,69	12,67	95,89	0,41
1440	29,539	0,027	0,160	58,330	0,09	100,00	41,68	12,31	93,29	2,65

Results of $^{40}Ar/^{39}Ar$ dating by step heating analysis of micas. The table gives isotopic data errors and age, with the experimental ^{39}Ar moles released and cumulative %^{39}Ar.

Whole rocks were crushed, sieved and individual grains chosen under a binocular microscope. All separates were irradiated at the Nuclear Ford reactor of the University of Michigan.The J factor was estimated by replicate analysis of the Fish Canyon sanidine standard with an age of 27.55 ± 0.08 Ma (Lanphere and Baadsgaard, 1997) with 1.5 % relative standard deviation. Interfering nuclear reactions on K and Ca were calculated by co-irradiation of pure salts with values of 40Ar/39ArK= 0.031 $^{37}Ar/^{39}ArCa$ = 0.000205 and $^{36}Ar/^{39}ArCa$ = 0.000781 for Michigan Ford Sampled were loaded in aluminium packets into a Staudacher type double vacuum furnace and step heated in a classical fashion, usually from 600°C to 1400°C . Feldspars were heated using a more evolved cycled protocol, following that suggested by Lovera et al. (1989). The gas was purified by means of cold traps with liquid air and Al-Zr getters. Once cleaned, the gas was introduced into a VG3600 mass spectrometer, and 2 minutes were allowed for equilibration before static analysis was done. Signals were measured using a Faraday cup with a resistor of 1011 ohm for ^{40}Ar and ^{39}Ar while ^{39}Ar, ^{38}Ar, ^{37}Ar and ^{36}Ar were analysed with a photomultiplier after interaction with a Daly plate. Blanks at 500°C, 1000°C and 1200°C are systematically measured for each mass between samples and extrapolated then substracted directly from measured signals for each temperature. Gain between collectors was estimated by duplicate analysis of 39Ar on both collectors during each analysis and also by statistical analysis over on a period of several years. This gain has an average value of 95 and is known at better than 1.5%. This error is included in the age calculation, along with analytical errors on each signal and errors on the blank values.

Table 3

Temperature °C	$^{40}Ar/^{39}Ar$	$^{38}Ar/^{39}Ar$	$^{37}Ar/^{39}Ar$	$^{36}Ar/^{39}Ar$ (10^{-3})	^{39}Ar (10^{-4}moles)	$F^{39}Ar$ released	$\%^{40}Ar^*$	$^{40}Ar^*/^{39}Ar$	Age Ma	± 1σ Ma
K1C20		K-feldspar		J= 0.00431						T 4.A
507	9,745	0,013	0,055	1,121	10,98	12,00	96,63	9,42	71,78	0,66
506	7,552	0,012	0,077	0,272	3,50	15,83	99,00	7,48	57,22	0,54
546	7,607	0,012	0,060	0,291	1,74	17,73	98,92	7,53	57,59	0,74
546	7,608	0,012	0,012	0,062	1,39	19,26	99,77	7,59	58,07	0,22
587	7,653	0,012	0,012	0,158	1,38	20,76	99,40	7,61	58,20	0,56
588	7,932	0,012	0,004	0,325	1,37	22,26	98,79	7,84	59,93	0,27
636	8,057	0,011	0,000	0,317	1,36	23,74	98,84	7,96	60,88	0,50
635	7,956	0,012	0,000	0,172	1,19	25,05	99,36	7,91	60,44	0,35
683	8,052	0,012	0,014	0,347	1,28	26,45	98,74	7,95	60,78	0,46
684	8,177	0,011	0,000	0,293	1,22	27,78	98,94	8,09	61,83	0,22
733	8,478	0,012	0,002	0,572	1,46	29,38	98,01	8,31	63,48	0,62
734	8,917	0,012	0,006	0,834	1,64	31,17	97,24	8,67	66,19	0,32
787	9,438	0,012	0,007	1,135	2,30	33,68	96,45	9,10	69,43	0,53
785	9,702	0,013	0,012	1,215	2,72	36,65	96,31	9,34	71,23	0,26
784	9,803	0,013	0,007	1,206	3,45	40,42	96,37	9,45	72,00	0,18
690	9,757	0,012	0,000	0,431	0,29	40,74	98,69	9,63	73,37	1,20
736	9,663	0,014	0,000	0,667	0,45	41,23	97,96	9,47	72,14	0,89
786	9,751	0,013	0,000	1,205	1,18	42,52	96,35	9,39	71,61	0,67
838	9,561	0,013	0,000	1,031	3,47	46,32	96,81	9,26	70,58	0,43
894	9,825	0,012	0,000	1,002	1,56	48,03	96,99	9,53	72,62	0,89
950	10,026	0,013	0,000	0,827	2,82	51,11	97,56	9,78	74,50	0,89
1007	10,432	0,013	0,000	0,834	4,69	56,25	97,64	10,19	77,51	0,34
1062	10,713	0,013	0,000	1,005	7,90	64,88	97,23	10,42	79,23	0,40
1117	10,993	0,013	0,005	1,096	15,64	81,99	97,06	10,67	81,11	0,35
1232	11,165	0,013	0,000	1,084	9,53	92,42	97,13	10,84	82,41	0,49
1443	11,124	0,013	0,000	1,289	6,93	100,00	96,58	10,74	81,65	0,81

Temp °C	Time min	f	D/r^2	1000/T (K^{-1})	$-\log(D/r^2)$	$\log(r/r_o)$
E= 36847.66 cal/mol ± 2353.15						T 4.B
$\log(D_o/r_o)$= 2.0/s ± 0.42						
507	20	12,00	9,43E-06	1,282	5,025	-1,647
506	30	15,83	4,65E-06	1,284	5,332	-1,501
546	20	17,73	4,17E-06	1,221	5,380	-1,224
546	30	19,26	2,46E-06	1,221	5,609	-1,110
587	20	20,76	3,95E-06	1,163	5,404	-0,978
588	30	22,26	2,81E-06	1,161	5,552	-0,899
636	20	23,74	4,46E-06	1,100	5,350	-0,753
635	30	25,05	2,78E-06	1,101	5,556	-0,654
683	20	26,45	4,73E-06	1,046	5,325	-0,547
684	30	27,78	3,15E-06	1,045	5,502	-0,455
733	20	29,38	5,98E-06	0,994	5,224	-0,389
734	30	31,17	4,73E-06	0,993	5,325	-0,334
787	20	33,68	1,07E-05	0,943	4,972	-0,311
785	30	36,65	9,12E-06	0,945	5,040	-0,284
784	60	40,42	6,34E-06	0,946	5,198	-0,209
690	60	40,74	5,61E-07	1,038	6,251	-0,054
736	40	41,23	1,33E-06	0,991	5,876	-0,051
786	40	42,52	3,54E-06	0,944	5,451	-0,075
838	84	46,32	5,26E-06	0,900	5,279	0,017
894	20	48,03	1,05E-05	0,857	4,978	0,040
950	20	51,11	2,00E-05	0,818	4,698	0,058
1007	20	56,25	3,61E-05	0,781	4,443	0,078
1062	20	64,88	7,55E-05	0,749	4,122	0,047
1117	20	81,99	2,26E-04	0,719	3,647	-0,072
1232	20	92,42	2,92E-04	0,664	3,534	0,093

Domains structure used for modelling
E= 50.00 kcal/mol, $\log D_o/r^2$=4.49 /s

T 4.C

domain	vol. fraction	relative size
1	0,14709	0,00007
2	0,02769	0,00025
3	0,03551	0,00051
4	0,0337	0,00139
5	0,14348	0,01076
6	0,32077	0,12713
7	0,28142	0,15478
8	0,01034	1

Results of $^{40}Ar/^{39}Ar$ dating by step heating analysis for K-feldspars K1C20. Table T4A gives isotopic data errors and age, with the experimental ^{39}Ar moles released and cumulative $\%^{39}Ar$. Ratios are corrected for blanks, analytical deviations and neutron interference reactions only. Table T4B gives diffusion parameters calculated during heating, with the inverse of absolute temperature (1000/T), and diffusion data for each step. Also shown are experimental activation energy -E- and frequency factor $-\log(Do/ro^2)$- obtained by linear regression on arrhenius plots with associated errors. Table T4C gives parameters used for the modelling of thermal history: activation energy -E-, frequency factor $-\log(Do/ro^2)$, number of domains, fraction of the total ^{39}Ar in each domain (total=1) relative size of each domain (compared to the biggest).

Table 4

T 5.A

Temperature °C	$^{40}Ar/^{39}Ar$	$^{38}Ar/^{39}Ar$	$^{37}Ar/^{39}Ar$	$^{36}Ar/^{39}Ar$ (10^{-3})	^{39}Ar (10^{-4} moles)	F ^{39}Ar released	% ^{40}Ar*	$^{40}Ar^*/^{39}Ar$	Age Ma	± 1σ Ma
K1C21		K-feldspar		J= 0.00431						
510	12,622	0,015	0,034	1,619	4,89	7,34	96,23	12,15	92,05	0,78
509	7,922	0,012	0,018	0,286	2,15	10,57	98,95	7,84	59,95	0,39
550	7,982	0,012	0,008	0,278	1,33	12,56	98,98	7,90	60,41	0,42
553	8,211	0,012	0,011	0,061	1,28	14,48	99,79	8,19	62,61	0,60
588	8,289	0,012	0,012	0,136	1,14	16,19	99,52	8,25	63,03	0,29
588	8,425	0,012	0,012	0,023	1,09	17,82	99,93	8,42	64,30	0,41
635	8,637	0,012	0,015	0,143	1,18	19,59	99,52	8,60	65,63	0,33
635	8,786	0,012	0,000	0,170	1,07	21,20	99,43	8,74	66,68	1,43
683	8,723	0,012	0,011	0,228	1,01	22,72	99,24	8,66	66,08	0,54
685	8,776	0,012	0,025	0,230	0,99	24,21	99,24	8,71	66,49	0,34
732	8,940	0,013	0,021	0,440	1,03	25,75	98,56	8,81	67,25	1,24
731	9,106	0,013	0,014	0,391	1,40	27,85	98,74	8,99	68,59	0,43
782	9,550	0,013	0,020	0,866	1,07	29,45	97,33	9,30	70,87	0,32
781	9,797	0,012	0,008	0,776	1,15	31,18	97,66	9,57	72,90	0,19
780	10,238	0,013	0,002	0,957	1,66	33,67	97,24	9,96	75,80	0,50
685	11,311	0,013	0,000	0,410	0,21	33,98	98,93	11,19	84,97	0,50
732	10,674	0,012	0,000	0,583	0,36	34,52	98,39	10,50	79,86	0,84
784	10,667	0,014	0,012	1,492	0,64	35,48	95,87	10,23	77,82	0,55
827	10,641	0,014	0,009	1,199	3,41	40,60	96,67	10,29	78,26	0,85
884	11,154	0,014	0,016	1,380	1,50	42,86	96,35	10,75	81,69	0,54
942	11,156	0,013	0,012	1,109	2,92	47,24	97,07	10,83	82,30	0,57
998	11,682	0,014	0,013	0,898	4,78	54,41	97,74	11,42	86,66	0,41
1052	12,184	0,014	0,011	0,794	6,21	63,73	98,08	11,95	90,61	0,44
1111	12,515	0,014	0,004	0,627	10,37	79,30	98,52	12,33	93,41	0,80
1226	12,255	0,014	0,004	0,657	8,27	91,72	98,42	12,06	91,42	1,07
1437	12,200	0,013	0,006	0,860	5,52	100,00	97,92	11,95	90,58	1,39

T 5.B

E= 36916.04 cal/mol ± 890.7
$\log(D_o/r_o)$= 2.05/s ± 0.16

Temp °C	Time min	f	D/r^2	1000/T (K^{-1})	$-\log(D/r^2)$	$\log(r/r_o)$
510	20	7,34	3,52E-06	1,277	5,453	-1,398
509	30	10,57	2,53E-06	1,279	5,598	-1,332
550	20	12,56	3,01E-06	1,215	5,521	-1,113
553	30	14,48	2,27E-06	1,211	5,644	-1,034
588	20	16,19	3,43E-06	1,161	5,465	-0,925
588	30	17,82	2,43E-06	1,161	5,615	-0,850
635	20	19,59	4,34E-06	1,101	5,363	-0,734
635	30	21,20	2,87E-06	1,101	5,542	-0,644
683	20	22,72	4,37E-06	1,046	5,360	-0,512
685	30	24,21	3,03E-06	1,044	5,518	-0,425
732	20	25,75	5,04E-06	0,995	5,298	-0,338
731	47	27,85	3,14E-06	0,996	5,503	-0,239
782	20	29,45	5,99E-06	0,948	5,222	-0,185
781	30	31,18	4,58E-06	0,949	5,339	-0,130
780	60	33,67	3,52E-06	0,950	5,453	-0,077
685	60	33,98	4,58E-07	1,044	6,339	-0,014
732	50	34,52	9,74E-07	0,995	6,011	0,019
784	30	35,48	2,92E-06	0,946	5,534	-0,022
827	94	40,60	5,43E-06	0,909	5,265	-0,007
884	20	42,86	1,23E-05	0,864	4,910	-0,005
942	20	47,24	2,58E-05	0,823	4,588	0,001
998	20	54,41	4,77E-05	0,787	4,321	0,014
1052	20	63,73	7,79E-05	0,755	4,108	0,037
1111	20	79,30	1,89E-04	0,723	3,723	-0,026
1226	20	91,72	3,09E-04	0,667	3,510	0,091

T 5.C

Domains structure used for modelling
E= 45.00 kcal/mol, $\log D_o/r^2$=4.00 /s

domain	vol. fraction	relative size
1	0,10012	0,00033
2	0,08445	0,00184
3	0,05408	0,00892
4	0,07283	0,05586
5	0,26861	0,18945
6	0,30453	0,20614
7	0,11539	1

Results of 40Ar/39Ar dating by step heating analysis for K-feldspars K1C21. Table T5A gives isotopic data errors and age, with the experimental ^{39}Ar moles released and cumulative % ^{39}Ar. Ratios are corrected for blanks, analytical deviations and neutron interference reactions only. Table T5B gives diffusion parameters calculated during heating, with the inverse of absolute temperature (1000/T), and diffusion data for each step. Also shown are experimental activation energy -E- and frequency factor $-\log(Do/ro^2)$- obtained by linear regression on arrhenius plots with associated errors. Table T5C gives parameters used for the modelling of thermal history: activation energy -E-, frequency factor $-\log(Do/ro^2)$, number of domains, fraction of the total ^{39}Ar in each domain (total=1) relative size of each domain (compared to the biggest).

Table 5

sample	Facies	method	mineral	age (Ma)	remark	reference
K89G181	undeformed two micas granite	Ar/Ar	biotite	87.5±0.4	plateau age	Matte et al., 1996
		Ar/Ar	muscovite	91.6±1.7	plateau age	Matte et al., 1996
K1C11	strongly deformed two micas granite	Ar/Ar	muscovite	100.7±1.3	plateau age	This study
K1C20	slightly deformed two micas granite	Ar/Ar	muscovite	103±1.3	plateau age	This study
K1C21	slightly deformed two micas granite	U/Pb	zircon	116.9±1	lower intercept	This study
		Ar/Ar	biotite	95.2±1.1	total fusion age	This study
K1L17	Dacite	U/Pb	zircon	98.7±1.4	lower intercept	This study
K1L23 & 24	Dacite	U/Pb	zircon	116.4±1.2	lower intercept	This study
K1L25	Dacite	U/Pb	zircon	103.9±2.3	lower intercept	This study
K1L26	Dacite	U/Pb	zircon	95.1±1.7	lower intercept	This study

Table 6: Geochronological data summary

Figures

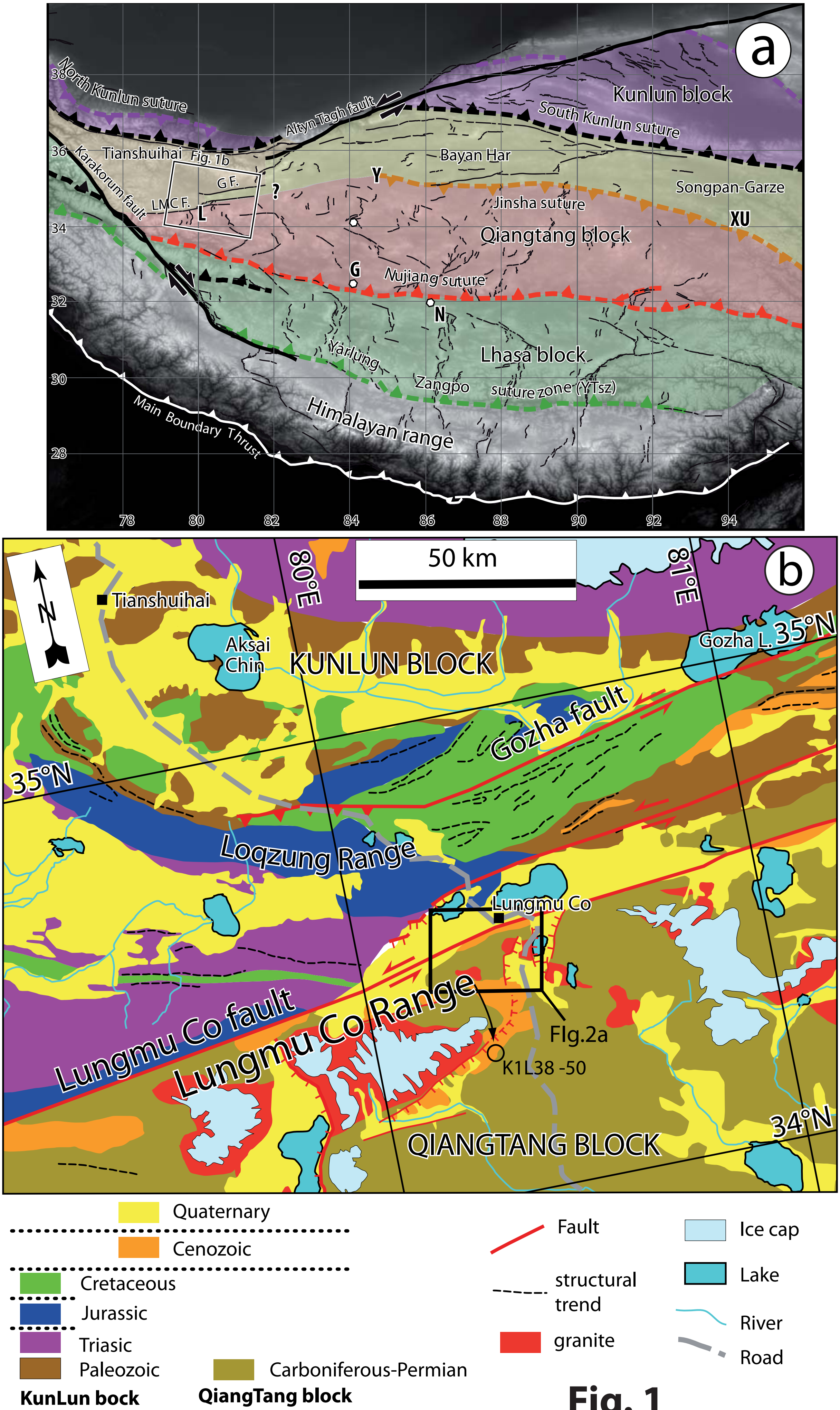

Fig. 1

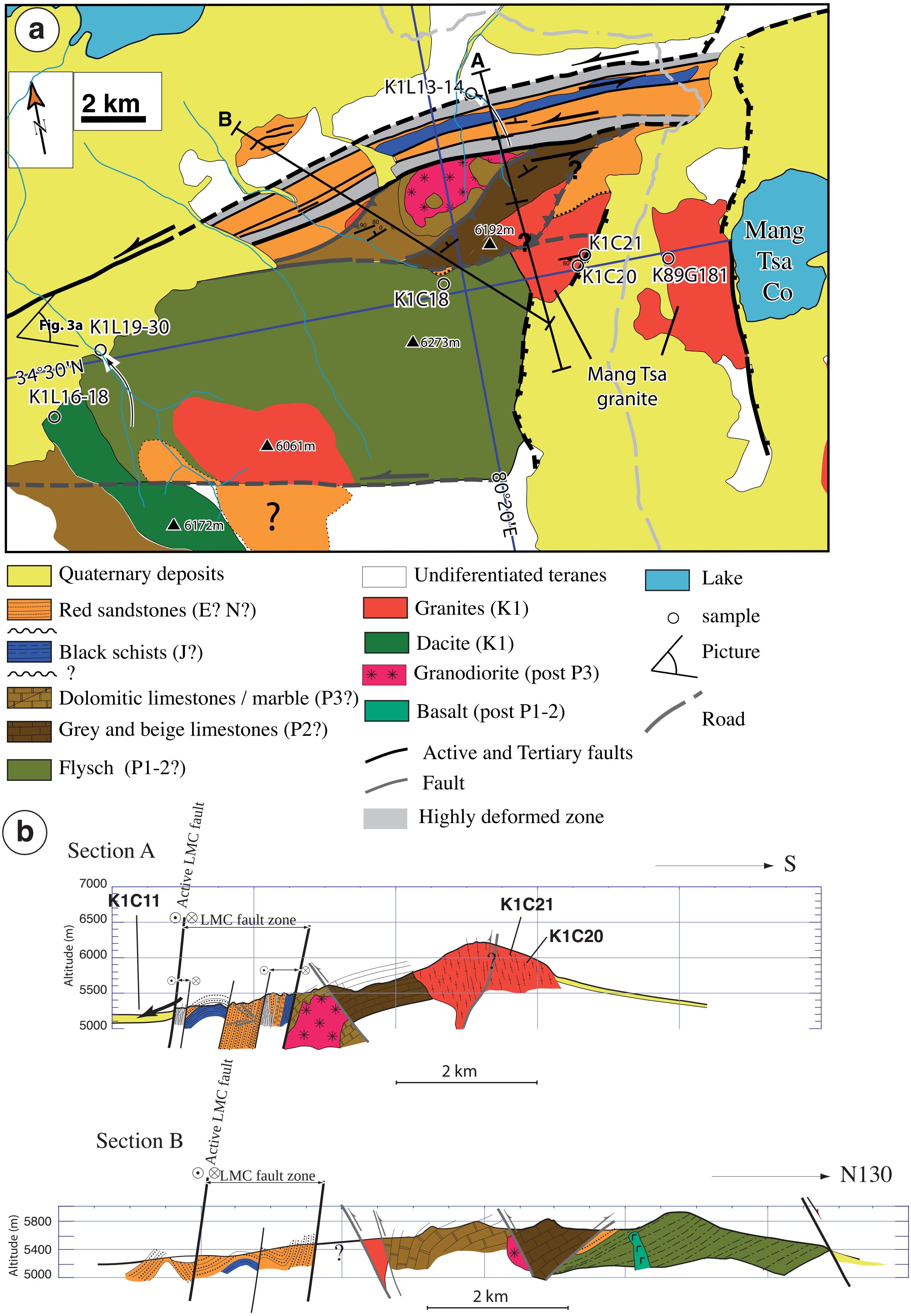
a
2 km
N
A
B
K1L13-14
6192m
K1C21
K1C20
K89G181
K1C18
Mang Tsa Co
Fig. 3a
K1L19-30
6273m
34°30'N
K1L16-18
Mang Tsa granite
6061m
80°20'E
6172m
?
Quaternary deposits
Red sandstones (E? N?)
Black schists (J?)
?
Dolomitic limestones / marble (P3?)
Grey and beige limestones (P2?)
Flysch (P1-2?)
Undiferentiated teranes
Granites (K1)
Dacite (K1)
Granodiorite (post P3)
Basalt (post P1-2)
Active and Tertiary faults
Fault
Highly deformed zone
Lake
sample
Picture
Road
b
Section A
Active LMC fault
LMC fault zone
K1C11
K1C21
K1C20
S
7000
6500
6000
5500
5000
Altitude (m)
2 km
Section B
Active LMC fault
LMC fault zone
N130
5800
5400
5000
Altitude (m)
2 km

Fig.2

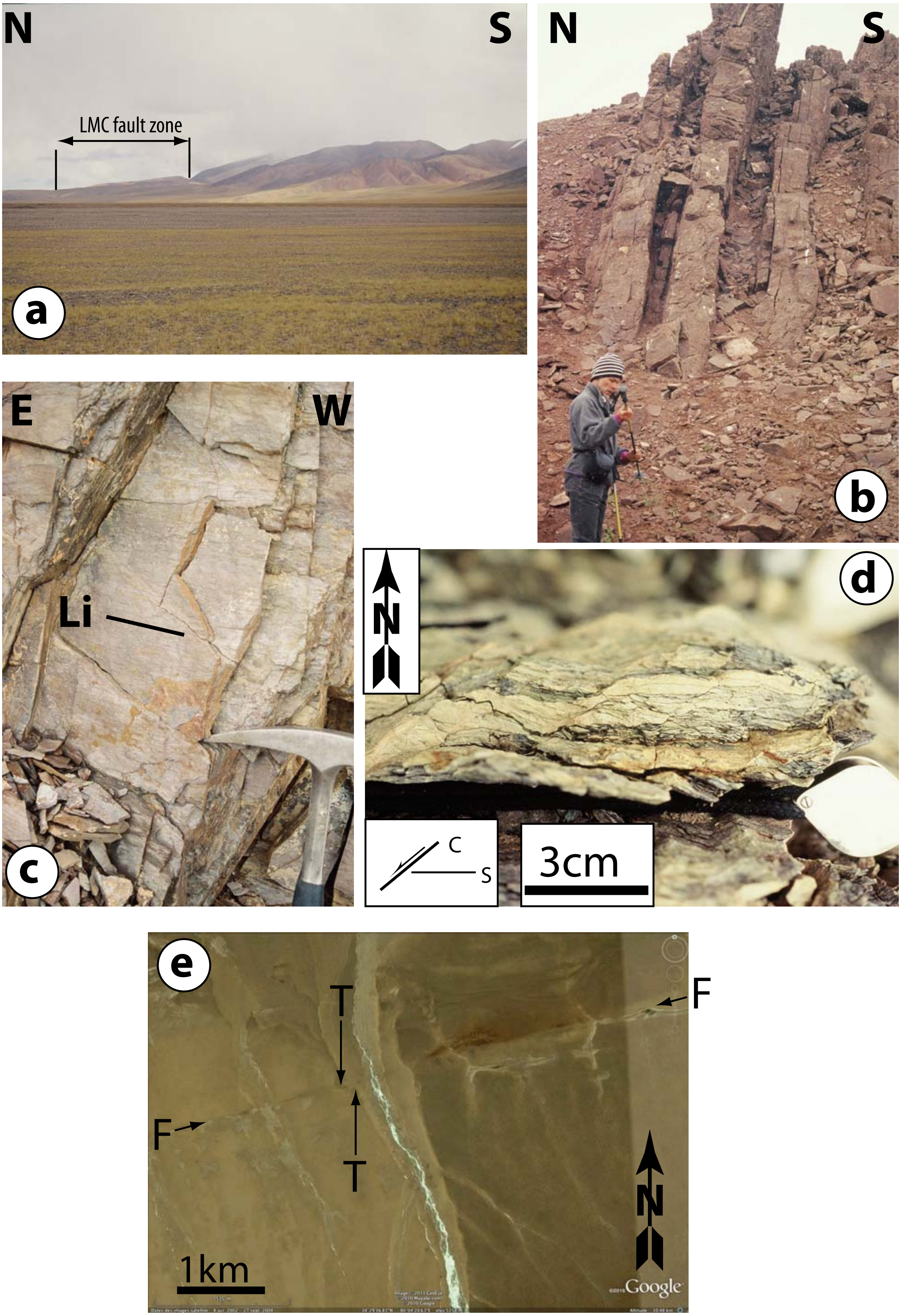

Fig. 3

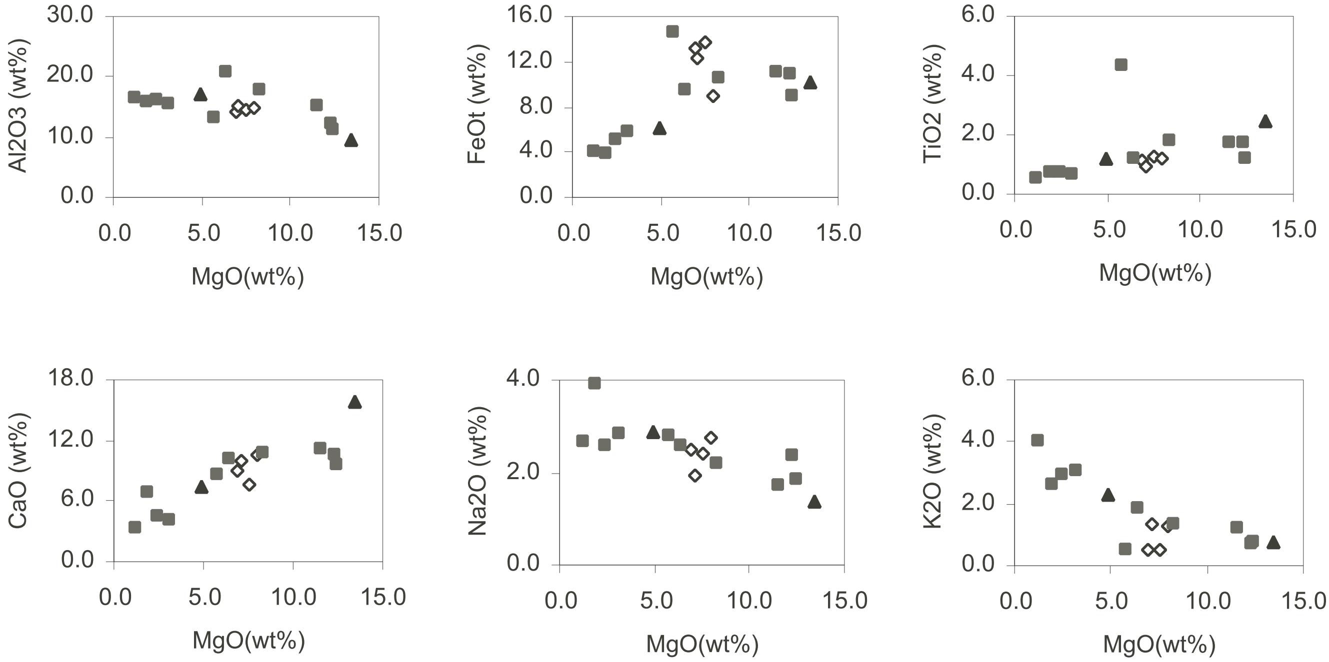

Fig. 4

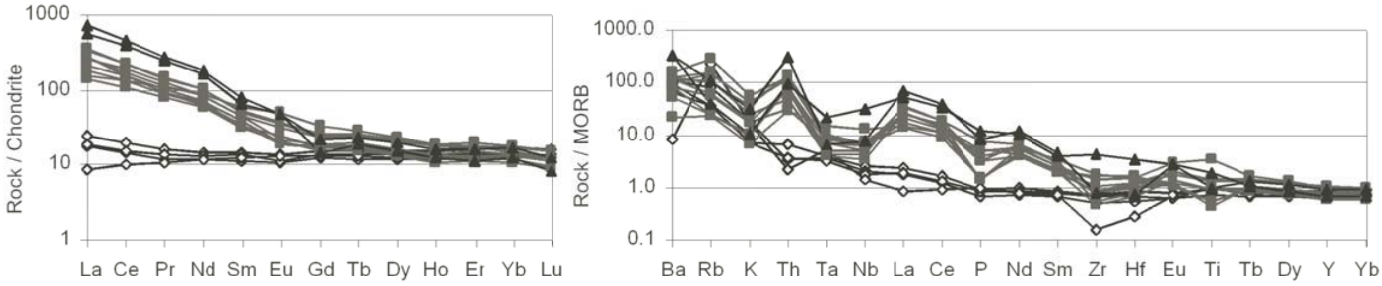

1000
100
10
1
Rock / Chondrite
La Ce Pr Nd Sm Eu Gd Tb Dy Ho Er Yb Lu
1000.0
100.0
10.0
1.0
0.1
Rock / MORB
Ba Rb K Th Ta Nb La Ce P Nd Sm Zr Hf Eu Ti Tb Dy Y Yb

Fig. 5

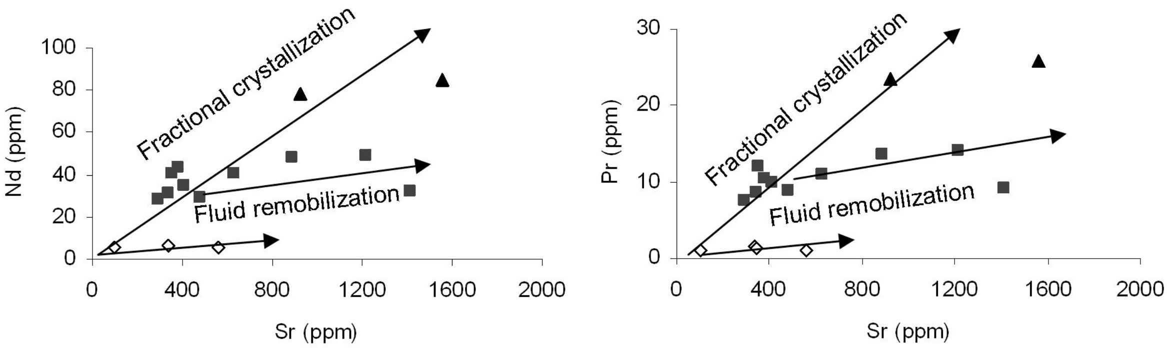
Fractional crystallization
Fluid remobilization
Nd (ppm)
Sr (ppm)
0
20
40
60
80
100
0
400
800
1200
1600
2000
Fractional crystallization
Fluid remobilization
Pr (ppm)
Sr (ppm)
0
10
20
30
0
400
800
1200
1600
2000

Figure 6

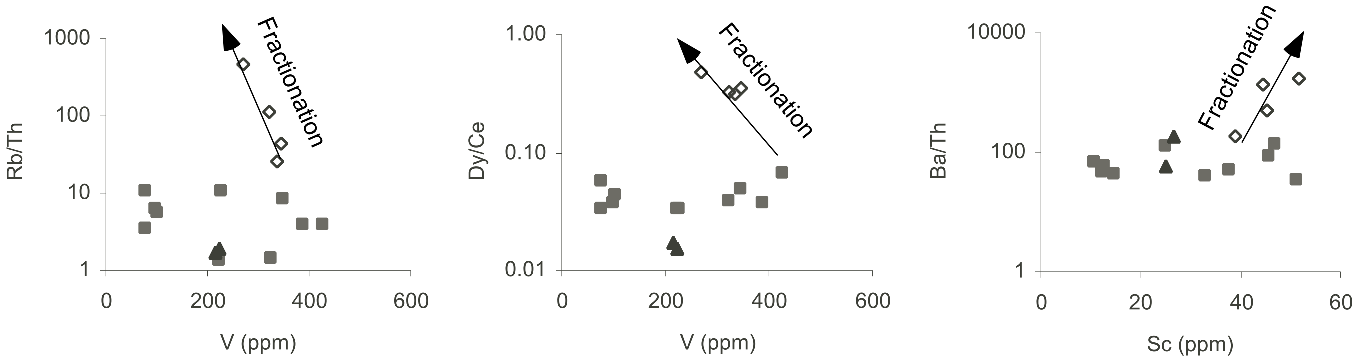

Fractionation
1000
100
10
1
Rb/Th
0
200
400
600
V (ppm)
Fractionation
1.00
0.10
0.01
Dy/Ce
0
200
400
600
V (ppm)
Fractionation
10000
100
1
Ba/Th
0
20
40
60
Sc (ppm)

Fig. 7

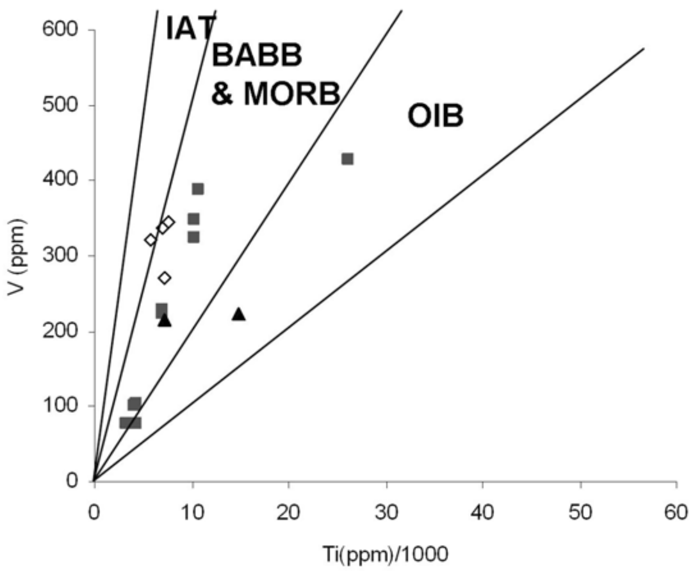
IAT
BABB
& MORB
OIB
600
500
400
300
200
100
0
V (ppm)
0
10
20
30
40
50
60
Ti(ppm)/1000

Figure 8

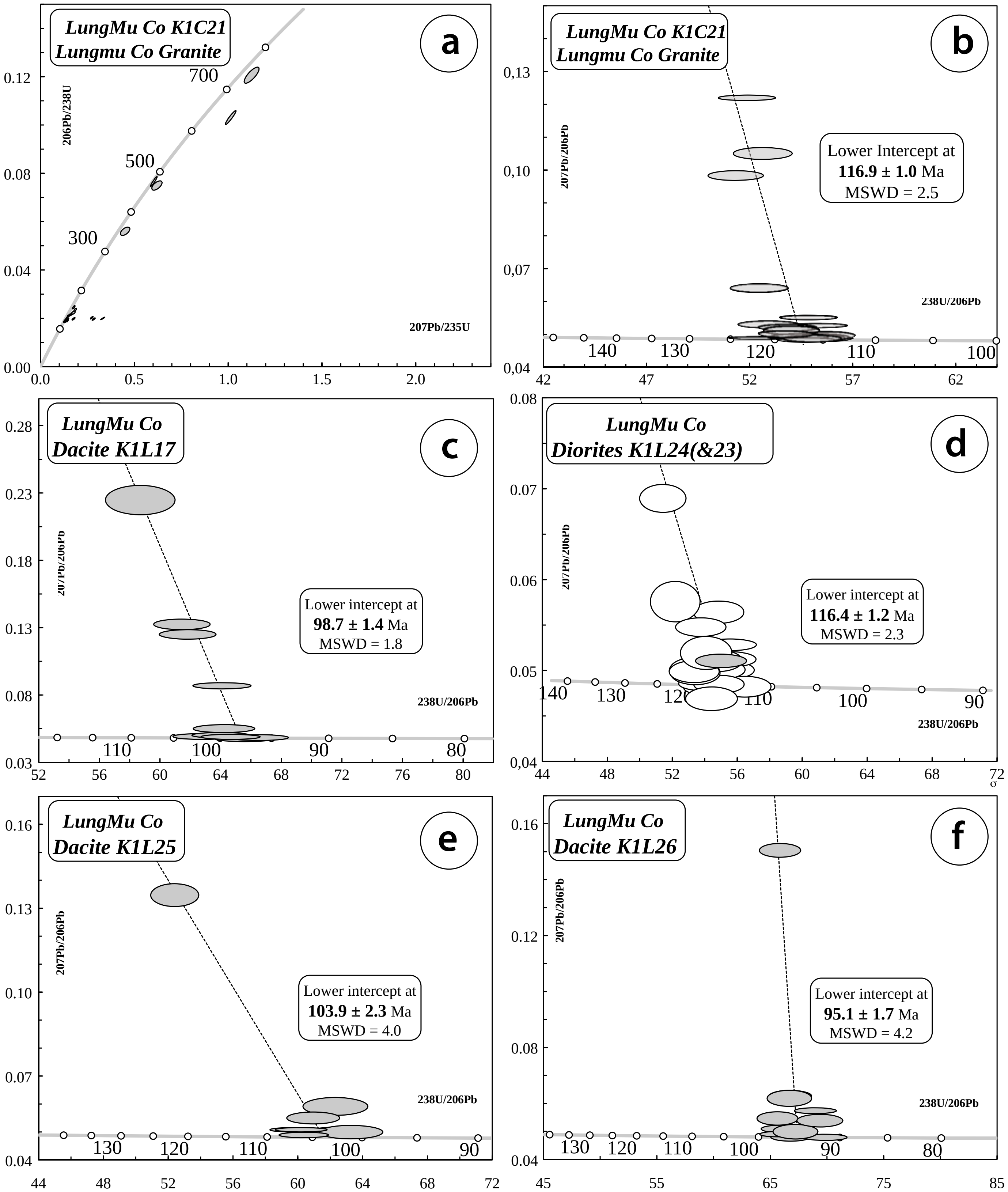
a
LungMu Co K1C21
Lungmu Co Granite
206Pb/238U
207Pb/235U
300
500
700
b
LungMu Co K1C21
Lungmu Co Granite
207Pb/206Pb
238U/206Pb
Lower Intercept at
116.9 ± 1.0 Ma
MSWD = 2.5
c
LungMu Co
Dacite K1L17
207Pb/206Pb
238U/206Pb
Lower intercept at
98.7 ± 1.4 Ma
MSWD = 1.8
d
LungMu Co
Diorites K1L24(&23)
207Pb/206Pb
238U/206Pb
Lower intercept at
116.4 ± 1.2 Ma
MSWD = 2.3
e
LungMu Co
Dacite K1L25
207Pb/206Pb
238U/206Pb
Lower intercept at
103.9 ± 2.3 Ma
MSWD = 4.0
f
LungMu Co
Dacite K1L26
207Pb/206Pb
238U/206Pb
Lower intercept at
95.1 ± 1.7 Ma
MSWD = 4.2

Fig. 9

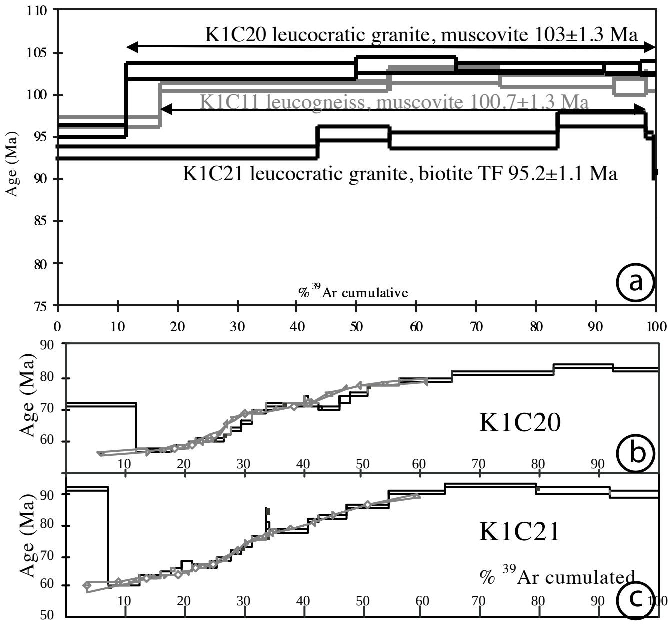

K1C20 leucocratic granite, muscovite 103±1.3 Ma
K1C11 leucogneiss, muscovite 100.7±1.3 Ma
K1C21 leucocratic granite, biotite TF 95.2±1.1 Ma
Age (Ma)
% 39Ar cumulative
a
K1C20
b
K1C21
% 39Ar cumulated
c

Fig. 10

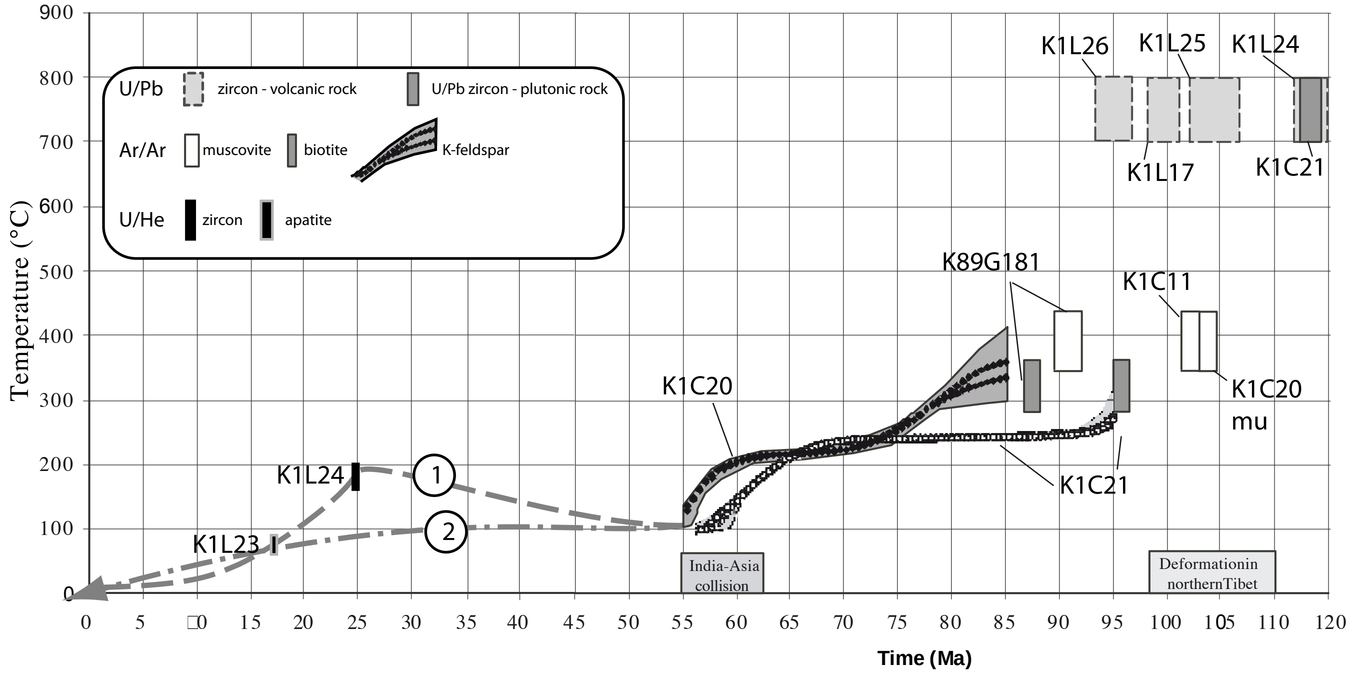

U/Pb
zircon - volcanic rock
U/Pb zircon - plutonic rock
Ar/Ar
muscovite
biotite
K-feldspar
U/He
zircon
apatite
K1L26
K1L25
K1L24
K1L17
K1C21
K89G181
K1C11
K1C20
K1C20
mu
K1C21
K1L24
K1L23
1
2
India-Asia
collision
Deformationin
northernTibet
Temperature (°C)
Time (Ma)

Figure 11

*Detailed Response to Reviewers

Dear Editor,

Please find below a transcript of the reviews of our paper that we have reorganized with numbers and of our responses (answer:) following each question.

Reviewer # 1 (resubmission and re-review)

R1-1) This manuscript deals with an area with very few geological constraints, in the western-central Tibet. The authors report new data concerning geochemistry, petrology and geochronology. Unfortunately these data are often over interpreted provided their quality (especially the U-Pb age) and, consequently, their interpretation is not rigorous. They finally present conclusions without objectivity, not based on their data, but on the their own feeling. Geochronology and geochemistry analyses have not been performed on same samples. Consequently, it seems very difficult to conclude from these data that the subduction zone described by the authors corresponds to the Jinsha subduction, which is located more to the east. According to the U-Pb age (300±200Ma) this subduction could be related either to the mid- Palaeozoic subduction occurring in the Kunlun to the North, or to the South to the Bangong-Nujiang subduction (Jurassic-Cretaceous)!

Answer: We aknowledge that the U/Pb data were of bad quality. We have since conducted new analysis on K1C21, as well as on several mafic rocks. The results are more precise and lead us to a different geodynamic conclusion. See also points R1-9, 15,16, 17, 19 and R2-1, R2-2, R2-4, R2-5 below

R1-2) As a second, important point, the authors decided to explain a 20°C/Ma cooling episode imaged on 2 Ar-Ar K feldspars models as a evidence for the onset of the India-Asia collision around 50-60 Ma. To satisfy their interpretation they rejected the HeZ data from Van der Beek et al., 2009 that does not allow the 20°C/Ma cooling event at 60 Ma. I acknowledge that the data of Van der Beek et al. is based on a single zircon aliquot instead of the usual 2 or 3 aliquots. However, the data is analytically good (correction factor Ft of 0.79) and the He Z age is perfectly consistent both with the other ages obtained in the study and with the HeA age obtained on the exact same sample. I thus consider that this data cannot be rejected and should be taken into account. If the HeZ age is considered then the last cooling event starts between 25 and 15 Ma.

Answer: We have Have sligthly changed our way to discuss the cooling history (see R1-8 below), but still feel that the data of Van der Beek et al.have to be taken with caution.

Relying on a single He zircon age, even if analytically good, is very dangerous. Zircon can present significant U and Th zoning in which case the ages between aliquots can present ages variations of about +/- 30% (Farley Annual review in mineralogy and geochemistry 2002). As this sample as only one aliquot we take it with caution. Furthermore the two (U-Th)/He age of Van der beck come from two different samples.

Comments on the regional geology (Chap. 2)

R1-3) In the geological frame, limits of blocks are not rigorously exposed. Figure 1a is unsuitable: - What is exactly the Tian Shui Hai block? - Where is the Bayan Har-Songpan Garzê terrane? Where are the Karakax and Gozha faults? And where is the Kudu suture? A schematic and clear frame of the sutures should be more convenient than Fig 1a. The authors could use and slightly modify the map already published

by the same team (Valli et al., 2008; Tectonics,vol27 TC5007, doi:10.1029/2007TC002184), which very clear.

Answer: **We have redrawn Fig. 1a with colours. We hope it is clearer now. Note that we have added the North Kunlun suture (Locally called Kudi suture) whilst it is not discussed in text.**

Comments on the geochemistry (Chap. 3 2)

- R1-4) Major element values in the text (line 189-192) do not correspond to the data reported in table 1. Are they re-calculated anhydrous data?

Answer: **This as been corrected. All the values are the raw values (i.e. not re-calculated on an anhydrous basis).**

- R1-5) Line 214: Transition between group 1, 2, 3 may result first from differentiation. Authors have to test by trivial diagrams choosing a highly incompatible element as differentiation index (for example Th) vs. La or La/Yb ratio, or, easier Th vs SiO2. They should compare LILE concentrations for a same degree of differentiation (same [Mg] or Th.).

Answer: **Actually there are no correlation between differentiation index such as MgO and Th and REE content or (La/Yb)n ratio. This has been precised in the text.**

- R1-6) Fig.6: How is the correlation line for Fractional crystallisation calculated? If this line goes through 0, both trace elements have to present the same or very close D values. It is not the case for Rb/Zr, Ba/Sr, Sr/Eu and Sr/Sm. A better choice would be Sm/Eu, Sr/Nd, Sr/Pr ...

Answer: **We have replaced the previous diagrams by Sr/Nd and Sr/Pr plots that display the same trends than the one previously observed in fig 6.**

Comments on the geochronology - thermochronology (Chap3 3)

- R1-7) As yet precised, dated samples are not the ones that have been analysed for geochemistry, and this generates first order data interpretation problems. For example, sample K1C21 that has been dated by the authors is interpreted as a subduction granite but no chemical composition (which would be the base to discuss the source of that rock) is given.

Answer: **The petrography of the granite (muscovite rich) as well as the presence of inherited zircon core suggest a crustal origin. Our new U/Pb data clearly indicate that the granite crystallization is coheval with the mafic magmatism (dacite, diorite) that is related with supra-subduction context. However the source of the mafic rocks and the granite are clearly different, but they are most probably related with the same thermal event. This as been precised in the revised manuscript.**

- R1-8) The cooling curve is not related to the same and unique sample: the three methods (U/Pb, Ar/Ar (micas and K-felds), U-Th/He (zircon, apatite)) have not been applied on the same sample. For example, sample K89G181 is separated from samples K1C21 and K1C20 by a normal fault (figure 2). Complete cooling curves built up to decipher the long term cooling history of a region should be obtained on single samples that can be compared through time and place. To my opinion it is very uncertain to draw a long term cooling curve using several samples some of them separated by faults.

Answer: **We agree with this comment and we have removed the cooling curve obtained comparing He and Ar data. We only calculate the mean cooling rate from our last Ar constrain to the surface, that shows**

that a period of very slow cooling must have taken place sometime after 55 Ma. In the discussion we added that such evolution is compatible with van der eek et al. (2009) interpretation of the Lung Mu Co He ages that suggest Paleocene/Eocene formation of the north-western Tibetan plateau.
see points R1-8 and 24 below.

U/Pb method:
R1-9)- Line 265: the authors contradict between text and table: "individual zircon" or "2 to 5 grains"? It is not the same thing.
- The validity of a fit relative to the individual error is measured by the Mean Square Weighted Deviation (M.S.W.D.). It is surprising that authors did not calculate this coefficient. When calculated, M.S.W.D. = 62083!!! With such a value, no conclusion concerning lower and upper intercepts can be driven. Sometimes, analysts have to accept that points do not align...
Answer: As stated above, all this section has been changed with new U/Pb data.

Ar-Ar method:
- R1-10) Line 271: K89G181 Muscovite: Authors do not precise that the age has already been published in Matte et al. (1996).
Answer: This is now clearly stated in the text.

- R1-11) The K1C11 muscovite age spectrum is presented (Fig.8). No relation to this age is given in the text. Moreover, this sample is extracted from a moraine and was thus not collected in its original place... and it is the only strongly deformed sample (line 262). What interpretation can we derive from this data? Age of deformation? Cooling Age? No meaning?
Answer: We now present K1C11 muscovite age in section 3.3 and it is discussed together with the other ages in section 4.2.

- R1-12) The age spectrum K1C21 K-feldspar is not given. Why?
Answer: This was a mistake in the labels of Fig.8, as the two age spectra were labelled K1C20. The correct labels are on the new Ar/Ar figure.

- R1-13) Line 277: the first step is NOT excess argon. The age is older than the intermediate ones because they have suffered an argon loss.
Answer: How can the intermediate degassing steps show loss and not the first one ? That would be odd ! This type of degassing is typically known as representing the effect of excess argon most probably trapped in fluid inclusions decrepitating at low temperature during furnace heating

- R1-14) Line 282: the ages of 82 and 90 Ma are not the same as the muscovite age of 103 Ma
Answer: The phrase has been changed.

Comments on the discussion (Chap. 4)
- R1-15) Line 300: For the authors, the Kunlun/Tian Shui Hai block is equivalent to the Bayan Har terrane. In fact, Bayan Har-Songpan Garzê and Kunlun are two different terranes separated by at least the Permo-Triassic suture (Molnar et al., 1987, Sciences 235, 299-305; Burchfield et al., 1987, E.P.S.L.94, 57-70; Yang et al., 1996, Tectonophysics, 258, 215-231; Chang, 2000, International Geology review, 42, 813-831; Roger et al., 2003, Tectonics, 22, 4, 1037-1057;

Weislogel, 2008 Tectonophysics, 451, 331-345; Wang et al., 2009, Island Arc, 18, 444-466 and many other...)
Answer: There was a misunderstanding here, because what we called the Kunlun – Tianshuihai block located south of the South Kunlun suture is not the classical Kunlun (or Qaidam) block located to the north of that suture. To avoid this problem we now speak of the Tianshuihai terrane that his in continuity with the Bayan Har and the Songpan-Garze terranes south of the South Kunlun suture.

- R1-16 Line 299 to 302: How could a fault be equivalent to a suture?
Answer: If a fault offset a suture the two blocks can locally be in contact across the fault. We have added few words to explain how a suture can be "cryptic".

- R1-17) Line 304: the Jinsha suture is not the direct consequence of a simple collision between the North and South China blocks but between N China, S China, Kunlun-Qaidam, Qiangtang and Yidun blocks (Reid et al., 2007; Ore Geology Reviews, 31, 88-106; Pullen et al, 2008, Geology 36, 351-354; Weislogel, 2008; Roger et al., 2008, C.R.Geoscience 340,180-189 and many other...)
Answer: This has been precised

R1-18) Line 315-316: enigmatic sentence: If the authors look at the map of Matte et al. 1996, a huge massif outcrops to the north of the LMC fault (under the scale cartouche of the fig 1b). Moreover, dated granites in this paper are to the south of the LMC Fault.
Answer: We are not sure to understand the comment. Anyway this has been changed by the new U/Pb ages.

- R1-19) Line 311-313: The authors have no right to write: "The fact that we document basic rocks of probable Permian age corresponding to a supra-subduction zone setting in LMC range confirm that the Jinsha suture continues in the LMC area". The authors did not demonstrate that the granite K1C21 was a granite associated with a subduction zone, in fact no geochemical analysis was performed on this pluton. Furthermore, the emplacement of the granite is not dated (300 ± 200 Ma), this granite could be associated either with a Early Palaeozoic subduction (as the one of Kunlun suture) or a more recent subduction like the one associated with theBangong suture. As a conclusion, the Jinsha suture is not dated in this area or does not pass through this area.
Answer: Based on our new U/Pb ages we have totally revised this part. The mafic rocks as well as the granite are not related anymore with the Nujiang suture but rather with effect of the Lhasa bloc subduction below the Qiantang bloc.

- R1-20) Line 313-314: In the geological setting, the authors do not describe the presence of blueschists. Are there blueschists as in the Central Qiangtang?
Answer: No blueschists have been observed in this part of the Qiangtang bloc.

- R1-21) Line 334-335: The authors should give the closing temperatures of the minerals used for the cooling rate. What is the error bar on these proposed rates? If we calculate the cooling rate of the undeformed K89G181 granite (Matte et al., 1996) between muscovite and biotite, we find 25°/Ma, and not 10-15°C. Why such a strong difference?
Answer: We now give the closure temperatures.

R1-22) Concerning the deformed granite (K1C11; K1C20; K1C21), no calculation is possible on the couple muscovite-biotite, because the data were not obtained on these two minerals in each sample. Moreover, K1C11 comes from a moraine and its exact position is thus unknown.
Answer: We have removed the calculation

R1-23) Line 349-350: What are the error bars? Are these values representative?
And R1-24) Line 362: "The (U-Th)/He zircon age (Van Der Beek et al., 2009) even suggest a slight reheating". The sentence is misleading. For Van der Beek et al. (2009) "there is a tectonic and morphologic stability of the NW plateau since at least Eocene times, only 15-20 Myr after the onset of the India-Asia collision". If there is a slight reheating, what is its cause? The reheating is only suggested compared to the Ar data obtained in the present study. For more impartiality, the authors should also discuss the hypothesis that the cooling occurs at only 17-25 Ma as the cooling curve should show if U-Th/He zircon data are taken in account. The 20°C/Ma cooling around 60 Ma is estimated based on Ar Ar models for which no error bars are provided. What is the reliability of this data provided that it occurs in the final stage of the model? This should at least be discussed. If this relatively strong increase in cooling rate (5 times) was registered along the LMC fault, should we not expect to find it elsewhere, for example along the Altyn Tagh or Karakax fault? Such information are not discussed in the manuscript.
Answer: The error bar is given by the gray area on Fig. 11 (see figure legend). We think that the rate increase is significant.

- R1-25) Spelling of local names is extravagant and extremely variable (Tian Shui Hai, Longmu Co, Qiangtang, Bayan Har, Kunlun, Altyn Tagh ...)
We have carefully checked from the 2004 geological map of Tibet. We now use Tianshuihai, Lungmu Co, Qiangtang, Bayan Har, Kunlun, Altyn Tagh, Songpan-Garze

- R1-26) Another point is the improvement of the English and the correction of the many misspellings. The manuscript should be proof-read in details and the English should be check by a native speaker.
Answer: We have done our best. Our english his far from perfect, but reviewer n°2, a native speaker, think that "The manuscript is exceptionally well written, was mostly a pleasure to read".

In summary, this manuscript cannot be published as it is and I suggest a complete rewriting before a new submission.

Reviewer # 2 (moderate revision)

Successive deformation episodes along the LungMu Co zone, west central
Tibet.
By Leloup et al. submitted to Gondwana Research
Review by Michael Flowerdew

This paper presents the results of new field observations, mapping, geochemistry and geochronology from rocks collected from a remote and difficult to access region of northwest Tibet. The LungMu Co fault zone, which runs through the region, is inferred to represent the boundary between Laurasian and Gondwanian terranes. The tectonic significance of this boundary is derived from new geochemical data on intermediate and mafic volcanic and igneous rocks and geochronology of granitoid rocks which are variably affected by ductile deformation associated with movement along the fault zone. Ar-Ar cooling ages from mica forming foliations, K feldspar and U-Pb zircon geochronology from deformed granitoids are used constrain the deformation and exhumation history. It is inferred from these data that an early phase of deformation relates to a suturing between the Gondwanan and Laurasian terranes in the Jurassic, slow cooling and exhumation in the mid-Cretaceous and a second phase of uplift and cooling at about 60 Ma,which is related to India - Asia collision. As a reader not familiar to the intricacies of Tibetan tectonic evolution, my review is very much as a 'cold' reader. The manuscript is exceptionally well written, was mostly a pleasure to read. The geochemical data are well presented and carefully discussed and the Ar geochronology is good quality. These together with the field observations go some way toward supporting the revisions in the tectonic evolution of this remote area. There are in my view areas where the paper can be improved and some of the evidence is lacking from the data reported, in particular regarding the U-Pb data.Listed below are some of the main points for consideration, and I also include an edited PDF of the manuscript with further comments the authors may wish to consider. Finally, I wish the authors every success in their revisions and invite them to contact me should any point need further clarification.

R2-1) U-Pb zircon data. Whilst the U-Pb zircon geochronology is not in any instance of poor quality, unfortunately the high level of discordance, in my view, means the data should not in any way be interpreted as meaningful. While the authors acknowledge the data result in 'badly defined' emplacement age of 300 ± 200 Ma emplacement age, I quite strongly disagree, and hesitate to draw any significance to this data. I would therefore suggest the data be removed from the manuscript as it offers little scientific value.
Answer: **As stated above, all this section has been changed with new U/Pb data.**

R2-2) The authors state (line 290) that that granite contains inherited Proterozoic grains, and infer the grains may be 2.4 Ga, on the basis of the upper intercept and the presence of cratonic material of that age to the north. Given the age intercepts are defined from fractions with different morphologies, different degrees of abrasion and different colour, difficulty in assigning the degree of ancient or recent Pb loss, it is clear that the each analysis point does not record a form a simple mixing line between zircon that grew during granite crystallisation and a 'Proterozoic' inherited population. The authors somewhat contradict themselves by stating many of these points in lines 265-267. The inherited grains could in my view easily be detrital grains incorporated into the melt during emplacement or intrusion from the flysch series country rocks and is as likely as their origin from any cratonic basement / source region. Any isochron calculated through these data is meaningless. CL images of zircon interiors may help confirm a detrital vs. basement origin for the inherited grains, but cannot address the potential for varying degrees of ancient / recent Pb loss. An in-situ technique or alternatively a chemical abrasion approach would likely be necessary to date this rock.
Answer: **Again, all this section has been changed with new U/Pb data.**

R2-3) Age of deformation affecting the granite. The authors in my view do not present enough evidence to suggest the deformation affecting the granite is shortly after emplacement. If that were the case I might expect more homogeneous deformation of the granitoid.

Perhaps another line of evidence could be through examination of the host country rocks. Surely the cleavage-porphyroclast relationships in the andalusite-bearing schists/slates would help interpretation. If the andalusite grew prior to the main foliation in the country rocks this would mitigate against a deformation at the time of intrusion, and vice versa.
Answer: **We unfortunately do not have more tectonic observations. We are more cautious and that point that is rather minor in our conclusions.**

R2-4) **Age of the basic series and linking the geochemistry with the geochronology.**
It's a shame the same samples on which the geochemistry was completed were not selected for geochronological investigation. The age of the mafic rocks are ascribed as Permian in age (line 311) yet I struggle to find any evidence for this other than the diorites which cut these rocks (?) have yielded c. 100 Ma Ar-Ar ages on mica, and so must at least be mid-Cretaceous or older. Is there any fossil evidence?
Answer: The new U/Pb ages of the basic give a new perspective to that problem.

R2-5) **The geochemistry of the dacites and diorites are not discussed nor are they mentioned in the conclusion. This seems odd as the bulk of the paper describes the geochemical results.**
Answer: **The geochemistry of the dacite is discussed and included in the conclusions.**

R2-6) **Paper readability. The geochemistry is very well written and pitched at a level where non-geochemist specialists can follow and understand. I feel that the tectonic overview is not quite so conducive for workers, like me, who are not that familiar with the tectonic development of Tibet. The authors should take the opportunity to state the importance of the many structures they refer to, such as the Karakorum Fault and make clearer both the context and the reasoning as to why it is so important to understand the timing of the LMC evolution.**
Answer: **We have added some sentences to present the Karakorum and Altyn Tagh faults.**

R2-7) **Diagrams. The colours used on the two maps are garish, not easy to read, and I strongly recommend the authors redraft these. In particular I cannot easily distinguish between the dacite, high deformation zone and red sandstones which are all similar greens shades on Fig 2. In my view, colouring according to stratigraphic age (as on Fig 1) does not translate to the lithological map of Fig 2.**
Answer: We have completely changed the figure 1 and 2 colour chart. We hope it is now clearer.

Answer to the Main remarks within the Pdf file (all other remarks have been taken into account).
Line 48. **Two sentences have been added about the LMC fault and its relationship with the Karakorum and Altyn Tagh faults.**
Line 71. **The figure 1a and the text have been modified to better explain the significance of the various bocks.**
Line 180. **Mafic has been substituted to basic.**
Line 273. **All discussions on the Ar ages are now in section 4.**
Line 330. **The age spread does not result from excess argon as the inverse isochrone ages have been calculated for each age. It is probably linked with local and episodic magma intrusions as suggested by the mafic rocks that show approximately the same spread in age.**

Line 377. **The geochemistry his now clearly stated in the conclusion.**
Line 387. **This conclusion has been removed from the main conclusions of the paper.**
Figures 1 & 2. **Colours have been changed.**
Figure 2. **Some samples are shown on Fig. 1b and the picture indicated corresponds to Fig. 3a.**

Successive deformation episodes along the ~~LungMu~~Lungmu Co zone, west-central Tibet.

Leloup P.H.[1], Arnaud N.O.[2], Mahéo G.[1], Paquette J.L.[3], Guillot, S.[4], Valli F. [5], Li H.[5 &6], Xu Z.[6], Lacassin R.[5], and Tapponnier P. [5].

1 : Laboratoire de Géologie de Lyon: Terre, Planètes et Environnement, UMR CNRS 5276, Université Claude Bernard – Ecole normale supérieure de lyon, 2 rue Raphaël Dubois, 69622 Villeurbanne, France.
herve.leloup@univ-lyon1.fr
2: ISTEEM-UM2, Géosciences Montpellier, UMR CNRS 5243, Université des sciences et techniques du Languedoc, 4095 Montpellier cedex 5, France.
3: Laboratoire Magmas et Volcans, UMR CNRS 6524, Observatoire de Physique du globe de Clermont-Ferrand, 63038 Clermont-Ferrand, France.
4 : ISTerre, CNRS, University of Grenoble I, BP 53, 1381 rue de la Piscine, 38041 Grenoble cedex 9, France.
5 : Equipe de Tectonique, Institut de Physique du Globe de ~~Paris et Université Paris 7, 75005 Paris, France~~Paris, Sorbonne Paris Cité, Univ Paris Diderot, UMR 7154 CNRS, F-75005 Paris, France.
6: Institute of Geology, CAGS, 26 Baiwanzhuang Road, Beijing 100037, PRC

Abstract

Field study, thermochronology and geochemistry of the east ~~LungMu~~Lungmu Co (LMC) range highlight some of the geological events that shaped western Tibet. The LMC fault zone has long been interpreted as the boundary between the ~~Tian Shui Hai – Kun Lun block~~Tianshuihai terrane of Laurasian affinity and the ~~QiangTang~~Qiangtang block of Gondwanian affinity. In the LMC range, the Paleozoic series is intruded by the Mangtsa leucogranite whose zircon have a U/Pb age of 116.9±1 Ma and by mafic rocks with U/Pb zircon ages ranging from 116.9±1 to 95.1±1.7 Ma. Geochemistry of the ~~paleozoic basic~~mafic rocks~~outcropping south of the fault zone~~ indicates that they have been emplaced in a supra-subduction zone ~~setting. This confirms that the South dipping paleo-Tethyan Jinsha suture zone can be prolongated towards Western Tibet even if no ultrabasite have been found west of 84°E.~~setting, probably the ~~The Permian sedimentary series are intruded by granodiorites and leucocratic granites. One granite yields a badly defined emplacement age of 300±200 Ma (U/Pb, lower intercept), while~~north dipping Nujiang suture zone. $^{40}Ar/^{39}Ar$ micas ages of the granite indicate that cooling below ~350°C occurred between 105 and 85 Ma. $^{40}Ar/^{39}Ar$ K-feldspar data suggest a ~~second~~fast cooling event at 60-55 Ma, which we relate to the reactivation of the LMC suture zone as a thrust at the onset of the India – Eurasia collision.

The last, and still active, deformation event corresponds to left-lateral strike-slip faulting along the ENE-WSW LMC fault.

1 Introduction

Tibet, the highest and largest topographic plateau on earth, was essentially built ~~since at least the Middle Miocene~~during the Cenozoic (e.g., Harrison et al., 1992; Tapponnier et al., 2001). However, the precise timing and mechanisms of the plateau building remain highly debated. This is in part because the long geological history of Tibet is still poorly known especially in remote area such as central and western Tibet. In western Tibet, the highest part of the plateau at more than 5000m asl, essential information such as detailed stratigraphy, continuity of known sutures, offset of those structures by major faults and geochronological constraints are still lacking. In this paper we aim to present new structural, geochronological and geochemical data from the ~~LungMuCo~~Lungmu Co range in west-central Tibet (Fig. 1).

The Lungmu Co (LMC) range is a noticeable topographic ridge culminating at 6192m, located south of LMC lake that stands at an altitude of ~5100m (Fig. 2a). The northern flank of the range corresponds to the eastern extremity of the active left-lateral LMC fault that can be traced for more than 150 km towards the right-lateral Karakorum fault (Molnar & Tapponnier, 1977) (Fig. 1a). The Karakorum fault is interpreted as the western boundary of the Tibetan plateau but its precise initiation age, total offset and present day rate are still debated (e.g., Leloup et al., 2011; Robinson; 2010; Valli et al., 2008; Chevalier et al., 2005). The LMC fault appears to abut against the Karakorum fault, whilst it has been interpreted to offset that fault by ~27 km (Raterman et al, 2007). Towards the Northeast, strike-slip motion of the LMC appears to be transferred to the Gozha fault (Fig. 1b) that ultimately merges with the Altyn Tagh fault which bounds the Tibetan plateau to the north (Fig. 1a) (Molnar & Tapponnier, 1977; Peltzer & Saucier, 1996).

It has been proposed by Matte et al. (1996) that the LMC range also corresponds to the boundary between the ~~Kun Lun block~~Tianshuihai terrane to the north and the Qiangtang block to the south, marking the prolongation of the Triassic Jinsha suture (Fig. 1a).

The data presented herein document the geology of the LMC range shedding light on more than 300 Ma of its geological history and its role in plateau evolution.

2 Regional geology of the ~~Lungmu-Co~~Lungmu Co area.

2.1 The ~~KunLun and TianShiHaï blocs~~Tianshuihai terrane

North of the LMC range, the Ku~~nlun/Tienchuihaï block~~Tianshuihai terrane is characterized by Carboniferous greenschists and greywackes overlain by Permo-Triasic flyshoïd dark slates (Matte et al., 1996). These series are unconformably capped by marine Jurassic black shales, and Cretaceous conglomerates, red sandstones and limestones~~of Cretaceous age~~ ~~(Figure~~(Fig. 1b).

South of the LMC range the Permo-Carboniferous series consists in black shales, Tethyan fusulinids bearing limestone and quartzite horizons. Presence of diamictites suggests a Gondwanian affinity (Matte et al., 1996). Further south, near Domar, the Permo-Carboniferous series is overlain by Triassic conglomerates and Jurassic limestone, this latter being locally ~~disconformably overlained~~unconformably overlain by Cretaceaous-Paleocene sandstones and red conglomerates (Matte et al., 1996).

These stratigraphic differences have led several authors to propose that the LMC fault could correspond to the boundary between ~~a Kunlun/Tienchuihaï block lateral equivalent to the Bahay Har terrane and Songpan terranes,~~the Tianshuihai block to the north and the Qiantang block ~~respectively~~to the South (Matte et al., 1996; Norin, 1946; Sengör and Okurogullari, 1991) (Fig. 1a). In such interpretation, the Tianshuihai terrane ~~1991). The~~would constitute, together with the Bayan Har and Songpan terranes, a large block bounded to the North by the South Kunlun suture, the trace of a north dipping Permo-Triassic subduction. South of this block, the LMC would~~thus~~ be the western prolongation of the ~~north verging~~South dipping Triassic Jinsha suture described in ~~Central~~central and eastern Tibet (e.g., Roger et al., 2003). However, no ultrabasites have been found in the LMC area and the detailed structure and thermal history of the range are unknown. Furthermore, the zone is sliced by recent strike-slip faults that may have disrupted the initial relationships between the units.

2.2 The Lungmu Co and Ghoza faults

The Ghoza - LMC strike-slip fault zone~~branches out of the Altyn Tagh fault and abut against the Karakorum fault ~500 km further SW (Fig. 1a) (e.g., Molnar & Tapponnier, 1977; Armijo et al., 1986). The fault zone~~ corresponds to two distinct faults that connect through an extension zone north of the LMC range at midway of its total length (Fig. 1b) (e.g., Liu et al., 1991). These faults are poorly documented from field observation, whilst some ~~sections are clear in the morphology from remote sensing, and indicate a~~segments show clear morphological indications of left-lateral ~~sense of~~active shear (Fig. 3e) (e.g., Molnar & Tapponnier, 1977; Armijo et al., 1986; Liu et al., 1991; Raterman et al., 2007). From the apparent offset of geological formations seen on Landsat images, it has been proposed that the total LMC fault offset amount is of about 25 - 32km, and affects the Karakorum fault (Raterman et al., 2007). ~~Axis~~Axes of folds affecting the Cretaceous limestones trend NNW-SSE near ~~Tian Shui Haï.~~Tianshuihai . This trend swings counter clockwise by 60° when approaching the LMC (Fig. 1b). If this ~~swing~~bend is interpreted as ~~a fault-bend,~~due to fault-drag, it would suggests a minimum of ~50 km for the left-lateral offset.

3 The Lungmu Co range.

Our description of the Lungmu Co (LMC) range is based on two detailed field cross-sections (A & B, Fig. 2b), field observations around the range, and SPOT and Landsat ETM+ satellite image interpretation (Fig. 2a). Given the access difficulties some observations are based on rocks collected in streams coming down from the range (Fig. 1b; Fig. 2a).

3.1 Rock facies and general structure

The range encompasses two main granitoïd bodies, as well as some basaltic dykes. The sedimentary cover includes carbonates, a flyshoïd series, and a clastic series dominated by red sandstones. ~~Most stratifications dip~~Bedding dips mostly to the N-NE in the core of the range and become almost vertical on the Northern flank (Fig. 2b; Fig 3b). In this zone, the sedimentary rocks are affected by several steeply dipping faults trending ENE-WSW. Locally such faults isolate calcshist slivers. One sliver shows ~~schistosities~~cleavage trending N130 to N160 affected by numerous left-lateral shear planes trending N80 to N 120 and few right-lateral planes trending N130 to N145 (Fig 3d). In another sliver the ~~schistosity~~cleavage trends N97 75 N on average with an almost horizontal lineation (pitch ~10° W) (Fig 3c). Such deformation probably results from strike-slip motion along the still-active LMC fault, thus defining a ~1.5 km wide left-lateral ~~deformation~~shear zone (Fig. 2; Fig. 3a). The red sandstones and conglomerates rest unconformably on black schists and some schistose conglomerates ~~include~~bear angular schist clasts, suggesting that several deformation events may have succeeded through time. The red sandstones, of Neogene age (N_{1-2}) according to the Tibet geological map (Chengdu Institute of Geology, 2004), are affected by normal faults that have been tilted together with the stratification~~The Tibet geological map (Chengdu Institute of Geology, 2004) attribute a Neogene age (N_{1-2}) to the red sandstones.~~

(section A, Fig. 2b). ~~Red sandstones~~They are are also found in the core of the range, resting unconformably on the flyshoïd series and overthrusted by dark grey fossiliferous limestones (section B, Fig. 2b). From regional stratigraphy the limestones are attributed to the Permian of the Qiangtang block. Further to the ~~east,~~East, the limestones are intruded by leucogranites that show a steep E-W foliation. Towards the ~~south~~north the limestones are in a steep fault contact with dolomitic limestones that have been intruded by a granodiorite body. In map view, the thrusts appear to trend NE-SW and are bounded to the north by the LMC fault zone (Fig. 2a).

The flyshoïd series~~are~~ composed of the alternance of dark sandstone and slate, are affected by folds verging to the South and intruded by basaltic necks. From satellite image interpretation, similar series appear to occupy a wide area of the South LMC range~~culminating at 6273m~~ (Fig. 2a). South of this zone outcrops a~~NW-~~ NW-SE elongated body mapped as βμJ on the geological map (Chengdu institute of geology and mineral resources, 2004). Rocks sampled at the western extremity of this body (K1L 16-18, Fig. 2a) are dacite and andesite. A river flowing out of the range (Fig. 2a) allowed ~~a sampling of~~us to sample paragneisses, orthogneisses, gabbros, diorite, andesite and basalt (samples K1L19 to 30).

3.2 Granitoids: relationships with stratigraphy and deformation.

~~Two types of granites are distinguished within the LMC range.~~ A granodiorite body intrudes the dolomitic limestones ~~affected by a contact metamorphism. The granadiorite~~and caused contact metamorphism and marble formation. The granodiorite and the dolomitic marbles are deformed both by the LMC fault zone to the North and by a reverse fault to the South (section A, Fig. 2b).

East of the LMC range stands the ~4x4 km MangTsa leucocratic granite (Fig. 2a). The granite is offset by the active normal faults bounding the LMC range to the east, and covered by quaternary deposits in its central part. The ~~paragenesis is made off~~granite comprises quartz, perthitic K-feldspar, plagioclase (oligoclase, muscovite and subsolidus titano-magnetite surrounding biotite). Such petrology is indicative of a crustal origin. The granite is undeformed in its SE part (K89G181) and shows a steep ~E-W foliation to the NW (KC20 & KC21) (Fig. 2). Both plagioclase and K-Feldspar porphyroclasts commonly show recrystallized grains at their boundaries, producing a core-and-rim structure diagnostic of dynamic recrystallization. Observations in natural examples suggest that such dynamic recrystallization occurs at medium- to high-grade temperature conditions (400-600 °C) during deformation (Passchier and Trouw, 1996). Similarly quartz grains show dynamic recrystallization through subgrain rotation or grain boundary migration. These microstructures are typical at medium- to high-grade conditions (400-700°) (Passchier and Trouw, 1996).

Mica fish also show flexuous shape, symptomatic of boudinage and recrystallization at the edges at temperature higher than 250 °C (Stesky, 1978). Thus, the foliation corresponds to a relatively high temperature (> 400°C) deformation. One sample (K1C11, sampled in moraines on the north side of the LMC range) developed a lower temperature deformation superimposed on the relatively HT foliation~~-~~. This late deformation is characterized by the occurrence of secondary millimetric muscovite and kinking of the K-feldspar, quartz locally exhibit undulose extinctions typical of low-grade conditions below 300 °C (Passchier and Trouw, 1996). There is no evidence whether this deformation is only restricted to the granite or has a regional signification.

South of the LMC range, andalusite bearing samples K1L38, 42a and 50 (Fig. 1b) are related ~~with~~to contact metamorphism at ~500-550°C and ~2 – 3 kb (Hilairet, 2002). Such contact metamorphism probably occurred at the time of emplacement of the granites that can be seen on the landsat images (Fig. 2a). The same samples also show relict garnets and staurolite suggesting a previous metamorphic event with higher metamorphic conditions of 550-600°C and ~6Kb (Hilairet, 2002).

~~3.2~~3.3 *Mafic rocks: petrology and geochemistry.*

A large mafic body is ~~visible on the landsat~~mapped from on the Landsat images SW of the flyshoïd series (Fig. 2a). ~~It is composed of~~Rocks sampled at the northern extremity of that body are dacite (samples K1L16 ~~and~~to 17). Other mafic rocks~~outcrop within the flyshoid series and~~ have been sampled as pebbles in a river bed further east, probably coming from the southern part of the mafic body ~~at the foot of the range.~~(samples K1L19 to 30). They are basalt, diorite, dacite and amphibolitized diorite. The basalt (K1L27) presents altered clinopyroxene, microlite of plagioclase and ilmenite. Two types of diorites have been distinguished. Type A (K1L23, 22, 24, and 24b) are undeformed, medium grain, and contain green amphibole, plagioclase, ilmenite ± biotite + accessory minerals (apatite, monazite ± titanite). Biotite is a primary magmatic mineral and usually developed before the amphibole. Quartz is locally present (K1L24). Type B diorites (K1L29, 30, and 25a) do not contain any biotite nor accessory mineral. The dacites (K1L17, 26, 28a and 25b) are undeformed with a porphyritic texture characterized by magmatic amphibole, plagioclase and quartz ± biotite. All these samples are slightly retrogressed with the development of chlorite at the expense of biotite and amphibole, while plagioclases are partially sericitized. Amphibolitized diorites (K1L21, 28b, 47 and 48) show amphibole and plagioclase recrystallization under sub-solidus conditions. Secondary minerals ~~appear such as~~are titanite, quartz, ilmenite and locally calcite (K1L47, K1L48). Chlorite is sparse suggesting temperature of recrystallization above 350°C.

In order to discuss the genesis of the ~~basic~~mafic rocks, the chemical composition of 6 diorites (K1L22, 23, 24, 24b, 29 and 30), 1 basalt (K1L27) 4~~acidic~~ dacites (K1L16, 17, 25 and 26) and 5 amphibolitized diorites (K1L21, 28b, 46, 47 and 48) has been measured. Major elements and some transition elements (Cu, Cr, V, Ni, Co, Sc) were analyzed by X-ray fluorescence at the University of Lyon. Other trace elements (Rb, Sr, Ba, Th, U, Pb, Y, Zr, Nb, Hf, Ta, Zn, and Rare Earth Elements) were analyzed by ICP-MS at the ENS of Lyon. Loss on ignition (LOI) was determined by heating the sample at 1000°C for 30 minutes. Analytical results are presented in Table 1~~ in which weight % of oxides are recalculated to 100 % on an anhydrous basis~~.

SiO_2 and MgO contents of the samples range from ~~44.74 % (diorite) to 67.56% (dacite) and 1.22% (dacite) to 13.46% (diorite)~~42.35 % (amphibolite) to 66.60% (dacite) and 1.20% (dacite) to 12.74% (amphibolite) respectively. All the samples have a low to medium content in K_2O, TiO_2 and Na_2O ~~(0.54 – 4.05 %; 0.56 – 4.36%; 1.38-3.89%~~(0.48 – 3.99 %; 0.55 – 4.23%; 1.31-3.71% respectively) and medium to high concentration in CaO, ~~FeO, Al_2O_3 (3.39-15.91%; 3.84-14.65%; 9.56-20.70%~~Fe_2O_3, Al_2O_3 (3.34-15.06%; 4.06-15.79%; 9.05-19.85% respectively). Such chemical composition is characteristic of calc-alkaline to high-K calc-alkaline rocks. In plots of MgO, taken as a differentiation index, versus major elements (Fig. 4), all the major elements show either positive (SiO_2, Na_2O, K_2O, Al_2O_3) or negative (TiO_2, CaO, FeO) correlation with differentiation. Such relationship suggests that all samples belong to the same fractionation trend.

Based on the REE patterns (Fig. 5) three groups can be defined. (1) Horizontal patterns characterized by a slight depletion or enrichment in light REE (LREE) relative to heavy REE (HREE) with $(La/Yb)_n$ ratios between 0.7 and 1.43. This group contains type B diorites and some amphibolitized diorite (K1l28b, 29, 30 and 48). (2) Steep patterns characterized by a strong enrichment in LREE relative to HREE with $(La/Yb)_n$ ratios between 10.7 and 24.8. This group consists in type A diorites (K1L22, 23 and 24), basalt (K1L27), dacites (K1L16, 17, 25b and 26) and some amphibolitized diorites (K1L21 and 46). (3) Steep patterns characterized by the strongest enrichment in LREE relative to HREE with $(La/Yb)_n$ ratios between 42.3 and 43.5. This group consists in one type A diorite (K1L24b) and one amphibolitized diorite ~~(K1L47).~~

(K1L47). The transition between the different group does not appears to be correlated with fractionation as MgO contents overlap (6.56 to 7.78 wt% for group 1, 1.2 to 11.98 wt% for group 2 and 4.75 to 12.74 wt% for group 3).

All MORB-normalized spidergrams (Fig. 5) are characterized by enrichment in Large Ion Lithophile Elements (LILE) such as Ba, Rb, Sr and K relative to REE and High Field Strength Elements (HFSE). HFSE show a slight depletion relative to REE for group (2) and (3) only. Despite a similar HFSE content, such relative depletion is not observed for group (1) samples as the LREE content is significantly lower than in groups (2) and (3) samples. Groups (2) and (3) are also characterized by a strong enrichment in Th not observed in group (1) samples for similar MgO content.

LILE enrichment results from different processes. As these elements are very mobile, they could have been enriched by re-mobilization during sea floor hydrothermalism or metamorphism related to obduction and/or collision. Alternatively, their enrichment could also suggest that the mantle source of these rocks had been either previously and selectively metasomatized in a supra-subduction zone context (Tatsumi et al., 1986) or contaminated by sediments or continental crust. Finally, such enrichment can be related with fractional crystallization. The secondary mobility of LILE ~~(e.g. Ba, Rb or~~(by example Sr) can be evaluated by plotting their concentration against that of less mobile elements (Fig. 6) such as ~~HFSE (Zr) or REE (Sm, Eu) or against another LILE with a different mobility (Ba versus Sr, Fig. 6).~~REE (Nd, Pr). Two trends are observed. The samples with the lowest (but enriched compared to HFSE) LILE contents define a linear trend best explained by a fractional crystallization process. On the other hand, the samples with the highest LILE concentration are significantly shifted away from the fractional crystallization trend. Such a shift is indicative of secondary LILE re-mobilization probably during sea floor alteration or metamorphism. For the relatively less enriched samples (first trend), the LILE enrichment is primary. Effect of crustal contamination or fractional crystallization can be estimated by considering only the samples that lie along a fractional crystallization trend in the previous plots as other samples chemistry is modified by fluid circulation. Among these samples even the most primitive ones are highly enriched in LILE (SiO_2<52%). This observation is incompatible with fractional crystallization or crustal assimilation as the only factors controlling the LILE enrichment. However such processes could have contributed to the observed chemistry. Consequently the LILE enrichment observed in all samples is most probably related to the metasomatism of the mantle source in a supra-subduction zone context.

The differences between the three groups can be related with (1) fractional crystallization or (2) the existence of several metasomatized sources. As previously discussed, in plots of MgO versus major elements (Fig. 4) all the samples define the same fractionation trend. Differentiation by fractionation can be tested inusing plots of incompatible elements ratios versus compatible elements (i.e. V and Sc, Fig. 7). In such plot, compatible elements are taken as a differentiation index. Ratios between chosen incompatible elements usually do not change during partial melting or fractional crystallization, unless, fractional crystallization or preferential melting of some peculiar mineral phases occurs. If such event takes place the incompatible elements ratio willthen change with differentiation index. In our plots, incompatible elements ratios for groups (2) and (3) samplesincompatible elements ratios does not significantly change with differentiation (Fig. 7). On the contrary groups (1) samples define steep lines characterized by progressive depletion in Th or LREE (Ce) relative to LILE (Rb), HFSE (Ta) or HREE (Dy), starting with the incompatible elements ratios of groups (2) and (3) samples. This pattern is indicative of removal by fractional crystallization of a mineral phase for which Rb, Ta and HREE are incompatible and Th and LREE compatible. Such mineral phase could be monazite. Actually,petrology indicates that group (1) diorites lackbiotite and accessory mineral such as monazite and apatite, which are always present in group (2) and (3) diorites.

In conclusion, all the analyzed samples belong to the same fractionation trend and are related with the melting of a metasomatized mantle in a supra-subduction zone context. More precisely based on Shervai's (1982) discrimination diagram the studied mafic rocks show characteristics of rocks emplaced in a back-arc environment (Fig. 8).

3.33.4 Geochronology, thermochrology.

In order to constrain the timing of emplacement of the MangTsa granite and of the mafic rocks, zircons from six samples were dated by the U/Pb in-situ technique with a LA-ICP-MS at the Laboratoire Magma et Volcans, Clermont-Ferrand (France). U/Pb data are reported in Table 2 and Fig. 9. The details of the analytical volcanics as well and asmethods and settings are given in appendix A1. To constrain the subsequent thermal history fivethree samples were studied:dated with the $^{40}Ar/^{39}Ar$ at the geochronology laboratory of Geosciences Montpellier (Université de Montpellier 2, France):an undeformed muscovite rich leucocratic granite (K89G181)(Matte et al., 1996), two slightly deformed leucocratic muscovite and biotite bearing granites (K1C20 and K1C21), and one strongly deformed granite (K1C11 sampled in

~~moraines on the north side of the LMC range) (Figure 1c). Analytical procedures followed those described in Paquette et al., 1999 and Arnaud et al., 2003 for U/Pb and ^{40}Ar/^{39}Ar respectively.~~

(K1C11) (Fig. 2a). ^{40}Ar/^{39}Ar data are given in Tables 3, 4 and 5 and in Fig. 10. The details of the analytical methods and settings are given in appendix A2. Muscovites and biotites of an undeformed muscovite rich leucocratic granite (K89G181) were previously dated (Matte et al., 1996). A summary of the available geochronological data is given in table 6.

~~U/Pb dating of K1C21 (Figure 8a) shows an important scattering of individual zircons in the Concordia diagram, underlining~~Twenty-two U/Pb analyses of zircon rims from K1C21 define a Discordia line intersecting the Concordia at 116.9 ± 0.1 Ma (Fig. 9b). Five sub-concordant other data produce older ages scattering between 350 Ma to 740 Ma (Fig. 9a). This underline a strong and heterogeneous inheritance, ~~and possibly Pb loss. Although very imprecise, the~~coupled to moderate Pb loss. The data suggest that granite emplacement took place ~~during late Paleozoic times~~in the lower Cretaceous at 117 Ma and that some parts of the zircons were inherited from a basement ~~of ca 2.5 Ga.~~~800 Ma old. The occurrence of such inherited grain further attest for a crustal origin for the leucogranite.

Zircons from the dacites and diorites yield precisely-defined lower intercept ages ranging from 116.4 ± 1.2 Ma (K1L23 and 24 diorites), to 103.9 ± 2.3 Ma (K1L25 dacite), 98.7 ± 1.4 Ma (K1L17 dacite) and 95.1 ± 1.7 Ma (K1L26 dacite) (Fig. 9, Table 2, Table 6).

^{40}Ar/^{39}Ar ~~micas dating yields younger ages (Figure 8b).~~dating of micas also yields Cretaceous ages (Fig. 10). Muscovites display plateaus ages between ~~92 (K89G181)~~100.7 (K1C11) and 103 Ma (K1C20). K1C21 biotite with age steps climbing from 88 to 95 Ma and a total fusion age of ca 95 ~~Ma, is younger than the nearby K1C20 muscovite. K89G181biotite yields a plateau age of~~Ma. K89G181 muscovite and biotite yields respectively plateau ages of 91.6±1.7 and 87.5±0.4 (Matte et al., 1996)~~. These ^{40}Ar/^{39}Ar data indicate that K1C21 (and K1C20) cooling below ca 350°C, occurred in Late Cretaceous times, much later than granite emplacement. Cooling of the eastern undeformed granite took place 7 to 10 Ma after the deformed part of the granite.~~

K-feldspar age spectra are complex~~(inset of figure 2c)~~ with excess argon in the first step and similar patterns for both samples K1C20 and K1C21: a first pseudo-plateau at 60-57 Ma, then a regular increase towards ages of the coexisting micas ~~(figure 2c inset).~~(Fig. 10b,c). Such age spectra are typically associated with slow cooling of the feldspars. These age spectra can be modelled using volume diffusion equation (Lovera, 1992; Lovera et al., 1989). The resulting models ~~(Figure 8c)~~(Fig. 11) show a rather monotonous cooling, in agreement with the mica ages, from late Cretaceous times ~~down to~~until ca 55-60 Ma when both samples start to cool much more rapidly. At that time cooling increase by a factor of 5 to reach ca 20°C/Ma. Following this event, mean cooling rate to present time appears to be very slow, of about 2°C/Ma. However, the timing of the slowing down of the cooling cannot be constrained with our data.

~~Apatite (sample K1L23) and zircon (sample K1L24) (U-Th)/He age obtained by Van der Beek et al. (2009) are 17.2+/-0.6 Ma and 24.7+/-0.5Ma respectively. Note that the zircon age has been obtained from a single analyse.~~

4 Discussion: geological history of western Tibet

4.1 Proterozoic inheritance

Zircon from sample K1C21 show a Neo-Proterozoic inheritance, whilst very imprecise. Proterozoic ages in Tibet have already been reported, especially from the border areas such as the cratons of Tarim, Qaidam or ~~Songpan Garze.~~Songpan-Garze. It appears that most cratonic areas around Tibet especially in the North, and elsewhere in Asia have recorded several Proterozoic events at least 900 Ma old (Arnaud et al., 2003; Gehrels et al., 2003; Roger et al., 2003; Sobel and Arnaud, 1999). ~~Such an old Proterozoic basement (2.4 Ga) below central~~Our data suggest that a comparably an old basement (~800 Ma) exists below west-central Tibet and especially in ~~Qiantang~~Qiangtang. This extends further south the existence of a very old crust upon which ~~most~~a large part of Tibet would rest.

4.1 Lungmu Co suture.

The LMC fault zone has been assigned a position at the boundary between the ~~Kunlun/Tienchuihaï block~~Tienshuihai terrane (lateral equivalent to the Bahay Har terrane and the evermore eastern Songpan terrane) to the north, and the Qiangtang block (Matte et al., 1996) and then would be a the lateral equivalent of the Jinsha Triassic suture zone (e.g., Matte et al., 1996). In the absence of any ultamafic rocks, the suture was considered as "cryptic", the remnants of the suture zone being either eroded, buried or offset by later faults (e.g., Baud, 1989; Pan et al., 1992). In east Tibet, the Jinsha suture is associated with the last stage (lower Jurassic) of the so-called "Indosinian" collision between the South ~~China and North China cratons (~~China, North China, Kunlun, Qiangtang and Yindung cratons (e.g., Faure et al., 1999; Lin et al., 2000; Mattauer et al.,~~Faure et al., 1999; Lin et al., 2000; Mattauer et al., 1985~~ 1985, Roger et al., 2010). Roger et al. (2003) have documented the south dipping Indosinian

Jinsha suture as far west as Yushu (~97°E). More to the west, Permo-Towards the West, Permo-Triassic ophiolitic bodies are found along strike until ~90°E (Xijir Ulan lake). According to the Chengdu institute of geology and mineral resources (2004) geological map other ophiolites are found westward along strike at ~84°E, East and West of the Yanghu Lake (Y, Fig. 1a). The fact that we document basic rocks of probable Permian age corresponding to a supra-subduction zone setting in the LMC range (L, Fig. 1a), confirm that the Jinsha suture continues in the LMC area. The study area could then be theOur study suggest that no ultrabasic rocks outcrop westward equivalent of the Central Qiantang melange (Chen and Xu, 1986; Kapp et al. 2003).

Some undated granitoïds outcrop on the south side of the LMC fault, while they are absent north of the fault (Fig. 1b). On the geological map (institute of geology and mineral resources, 2004), they appear as granites, tonalite and granodiorite. These granitoïds shape the highest reliefs and intrude the Carboniferous and Permian sediments and could be a paleo-volcanic arc. In the LMC range, one of these granitoïds is a granodiorite with a contact metamorphism in the dolomitic limestones of probable Permian age (Fig. 2). Unfortunately, the age of the MangTsa granite is poorly constrained (300±200 Ma) and it cannot be deciphered if it emplaced during that subduction event.

Closure of the Jinsha suture is inferred to have occurred by the lower Jurassic (e.g., Roger et al., 2010). A similar age is compatible with the geology of western Tibet. Most Mesozoic rocks of the QianTang block have been eroded away along the LMC fault making direct correlations difficult (Fig. 1b), but Jurassic facies appear comparable North of the LMC fault and near Domar more than 100km to the south (Matte et al., 1996; Chengdu institute of geology and mineral resources, 2004).

4.2 Cretaceous cooling.

All micas ^{40}Ar/^{39}Ar ages of the MangTsa granite span in age between 87 and 103 Ma (Fig. 8b). Such ages correspond to the older ages of the K-feldspar (Fig. 8c). This suggest that temperature definitively dropped below ~350°C since the middle Upper Cretaceous in the LMC range. From the difference in age between the muscovite and biotite both the undeformed sample and the deformed ones appear to have cooled at ~10-15°C/Ma, but with an offset in time of 7 to 10 Ma. The fact that the undeformed part of the granite yields younger cooling ages than the deformed one suggest that deformation occurred prior to cooling below ~350°C, which is compatible with the textural mineral observations. In that interpretation, deformation would have occurred prior to ~100 Ma ago, possibly during late granite emplacement, given the large uncertainty on the MangTsa granite emplacement age.

From a tectonic and tectonic analysis, Matte et al. (1996) recognized three episodes of SSE vergent shortening: (1) ante Mid Jurassic; (2) post mid Jurassic and ante Cretaceous – Paleocene; and (3) Tertiary. While phase (1) can be related to the Jinsha subduction, deformations observed within the MangTsa granite are probably related to the phase (2). Such deformation is probably related with the Cretaceous collision between the Lhassa and QiangTang bocks along the Bangong-Nujiang suture zone (Fig. 1a) also recognized in the Central Qiantang (Kapp et al., 2007).in the LMC range making improbable a direct prolongation of the Jinsha suture zone towards the SW. This does not disprove, that the LMC zone is the present day boundary between the Tianshuihai terrane and the Qiangtang block but suggest that the suture is located further North and / or has been significantly offset by the Lungmu Co fault.

4.2 Cretaceous magmatism and cooling.

Our new U/Pb ages on Diorites, dacite and granite imply that a major magmatic event took place in the LMC area between 120 and 90 Ma (Middle Cretaceous). The mafic magmatism is indicative of a supra-subduction context and the granite results from crustal anatexis. So far these Cretaceous magmatic rocks are the only one known in northern Qiangtang area. More to the east, contemporaneous sub-aerial tuff and basalts have been described between Gerze and Nyima in southern Qiangtang bloc, as well as ~150 km further north (white dots on Fig. 1a) (Kapp et al., 2005). This magmatism is interpreted as being related with the final subduction of the Lhasa block beneath Qiangtang that ultimately resulted in the formation of the Nujiang suture (e.g., Kapp et al. 2005). The magmatic activity in the LMC area ~100 km north of the Nujiang suture (Fig. 1a), with diorites and dacites having back arc geochemical compositions (Fig. 8), could be due to back arc extension above that subduction.

Our mapping, as well as previous work (Matte et al., 1996), does not reveal mafic rocks nor cretaceous granite within the Tianshuihai terrane north of the LMC fault zone (Fig. 1b). This could be due to westward shift of potential outcrops by the LMC fault where no detailed field work has been performed so far. Another possibility, is that such potential magmatic rocks located on the southern egde of the Tianshuihai terrane have been underthrust below the northern Qiantang bloc in the location of what will later be the LMC strike slip fault. Actually Matte et al. (1996) recognized a post 100Ma north-south compression event in the LMC range. This event is contemporaneous with a compression event documented in southern Qiangtang following the cretaceous magmatic event (Kapp et al., 2005).

All micas $^{40}Ar/^{39}Ar$ ages of the MangTsa granite span in age between 87 and 103 Ma. Assuming closure temperatures of 390±45°C for the white micas (Hames and Bowring, 1994) and 320±40°C for the biotites (Harrison et al., 1985) a first-order cooling history of the Lungmu Co range can drawn (Fig. 11). After granite emplacement at ~117 Ma, temperature dropped below ~320°C in the Upper Cretaceous (95-90 Ma). This relatively long cooling time coincide with the timing of emplacement of the mafic rocks that span in age from ~116 to ~95 Ma (Table 6,Fig. 11). Cooling of the eastern undeformed granite (K89G181) appears to take place 7 to 10 Ma after the deformed part of the granite (K1C11, 20 & 21). This could suggest that deformation occurred prior to cooling below ~350°C, which is compatible with the textural mineral observations. In that interpretation, deformation would have occurred during late granite emplacement. However the age pattern is not confirmed by K1C20 Kf cooling history.

4.3 Cenozoic cooling: a far effect of the India-Asia collision ?

Taken altogether,~~all~~ thermochronologic data suggest a rather slow cooling since ~~the Cretaceous at ~4°C/Ma~~~85 Ma at ~3.5°C/Ma on average. However, diffusion modelling of K-feldspar data suggest an increase~~s~~ of the cooling rate to ~20°C at 60-65 Ma for both MangTsa granite samples (Fig. ~~8e).~~11). Such cooling rate is compatible with~~a broad,~~ tectonically driven exhumation event that could explain the erosion of the Mesozoic cover south of the LMC fault zone, but not north of it. This differential exhumation likely did not take place during the Neogene, as ~~Eocene~~Tertiary sediments outcrop at the same ~~altitude~~elevation on both sides of the LMC fault zone. This Paleocene exhumation episode may correlate with the Tertiary (Post ~60 Ma) faulting recognized ~~(Kapp et al., 2005) and~~by Kapp et al., (2005) in southern Qiangtang and the early Eocene continental subduction in Central Qiangtang (Roger et al., 2000).

~~Timing of~~Although age estimates for the India – Eurasia collision ~~vary upon the authors~~range between 65 and ~~40~~35 Ma (see Guillot et al., 2003 for a review)~~. However~~, most authors consider that ~~the collision~~it started between 55 and 60 Ma ago in Northwest Himalaya (e.g., Beck et al., 1995; Treloar & Coward, 1991; Guillot et al., 2008). This timing corresponds to that of the last ~~exhumation~~fast cooling in the LMC range (Fig. ~~8e)~~11) suggesting a causal link. Van der Beek et al. (2009) published (U-Th)/He ages of 17.2+/-0.6 Ma (apatite, K1L23) and 24.7+/-0.5 Ma (zircon, sample K1L24) for two diorite boulders of the LMC range. If taken into account in the cooling history, the zircon U-Th/He age could suggest a ~~After~~slight Tertiary reheating (path 1, Fig. 11). However, this age has to be taken with caution as it results from a single aliquot. The most likely hypothesis is that after 55 Ma, the cooling rate slowed down to less than~~0.5°C/Ma. The (U-Th)/He zircon age (Van der Beek et al., 2009) even suggest a slight reheating. However, as this age is based on only one measurement, and as the Cenozoic cover is very thin and discontinuous such reheating is unlikely. It is much more probable that the LungMu Co range experienced a very low cooling rate,~~2°C/Ma (path 2, Fig. 11), corresponding to a small ~~exhumation,~~degree of exhumation until recent time. This is compatible with ~~Such evolution would be coherent with~~the interpretation of Van der Beek et al. (2009) of the formation of the north-western part of the Tibetan plateau around Paleocene/Eocene time, together with the Kohistan and Ladakh, and its preservation since ~~then as suggested by van der Beek et al. (2009). In this context~~then. The formation of the northwest part of the Tibetan plateau could predate that of its north-central one, as paleo-~~the North Central one, as paleo-~~altimetric data suggest that ~~this~~the latter~~had~~ reached its present day elevation at ca. 35 Ma (Rowley & Curry, 2006; Dupont-Nivet et al., 2008), following increased exhumation rates at ~50Ma (Clark et al., 2010). This possible diachronism ~~in the~~of Tibet uplift could hypothetically be related with an earlier onset of collision in the west followed by an eastward growth (Tapponnier et al., 2001; Yin et al.,~~2002) in accordance with those proposing a collision at 60-~~ 2002). This would be compatible with studies proposing that collision occurred at 60-55 Ma in the west (Beck et al., 1995; Treloar & Coward, 1991) and around 50 Ma in~~its~~ central ~~part~~Himalaya (see Guillot et al., 2003 for review).

5. ~~Conclusion~~Summary of new hints on northwest Tibet geological evolution.

Our field ~~study in the easrten LungMu~~study, geochemical and geochronological analyses in the eastern Lungmu Co (LMC) range, immediately south of the LMC lake yield some hints on the tectono-magmatic evolution of one of the highest, poorly known part of the Tibetan plateau. It provides new constraints on the geodynamic evolution of western Tibet since the upper Paleozoic, whilst many of the conclusions await more detailed confirmations and additional field-studies.

The LMC fault zone corresponds to the boundary between the QiangTang block of Gonwanian affinity to the South and the ~~KunLun block~~Tianshuihai terrane of Laurasian affinity to the ~~north. It was the site of a South dipping subduction zone in the prolongation of the Yushu – Jinsha~~north but do not show ultrabasic rocks that would testify for a Paleo-Tethyan subduction ~~zone during the Permian.~~during the Permian. A major magmatic event occurred in the middle Cretaceous (117-95 Ma), with crustal partial melting generating the Mang Tsa leucogranite, and intrusion of mafic rocks. The geochemistry of the mafic rock indicates that they emplaced in a back arc setting probably north of and above the Nujiang subduction. We infer from field observation and thermochronological ~~This subduction yielded few granodioritic plutons and possibly middle pressure middle temperature metamorphism in the hanging plate (Qiang Tang). High temperature (≥ 400°C) deformation of leucocratic granites, occurred prior to ~100Ma, possibly at the time of emplacement. The LMC suture~~resuls that the LMC zone has been reactivated as a thrust at the onset of the India-Eurasia collision at ~60 Ma. ~~This~~South of the LMC fault this caused the erosion of the Mesozic cover and an exhumation of ~~several km south of the LMC fault,~~few km, probably at the time of the building of the ~~Northwesten~~northwesten Tibetan plateau. The LMC ~~suture~~zone has then been affected, and ~~reactivated by a~~possibly offset, by a en echelon series of WSW-ENE left-lateral strike-slip faults ~~in the prolongation of the Althyn Tagh fault,~~that connect with the Altyn Tagh fault, and that are associated with few N-S active normal faults.

Acknowledgements.

We are grateful to Michael Flowerdew and an anonymous reviewer for their comments. The fieldwork was financed by the French INSU Dyeti programm.

Bibliography

Armijo, R., Tapponnier, P., Mercier, J.L., Han, T., 1986. Quaternary extension in Southern Tibet: field observations and tectonic implications. Journal of Geophysical Research 91, 13803-13872.

Arnaud, N., Tapponnier, P., Roger, F., Brunel, M., Scharer, U., Wen, C., Xu, Z.Q., 2003. Evidence for Mesozoic shear along the western Kunlun and Altyn-Tagh fault, northern Tibet (China). Journal of Geophysical Research-Solid Earth 108, 2053, doi:2010.1029/2001JB000904.

Baud, A., 1989. The western end of the Tibetan plateau, In: Sengör, A.M.C. (Ed.), Tectonic evolution of the Tethyan region, Amsterdam, pp. 505-506.

Beck, R.A., Burbank, D.W., Sercombe, W.J., Riley, G.W., Barndt, J.K., Berry, J.R., Afzal, J., Khan, A.M., Jurgen, H., Metje, J., Cheema, A., Shafique, N.A., Lawrence, R.D., Khan, M.A., 1995. Stratigraphic evidence for an early collision between northwest india and asia. Nature 373, 55-58.

Beck, R.A., Burbank, W., Sercombe, W.J., Khna, A.M., Lawrence, R.D., 1996. Late Cretaceous ophiolite obduction and Paleocene India-Asia collision in the westernmost Himalaya. Geodinamica Acta 9, 114-144.

Cheng, J., Xu, G., 1986. Geologic map of the Gaize region with report. Chengdu, People's Republic of China.

Chevalier, M.L., Ryerson, F.J., Tapponnier, P., Finkel, R.C., Van Der Woerd, J., Li, H., and Qing, L., 2005, Sliprate measurements on the Karakoram fault may imply secular variations in fault motion: Science, v. 307, p. 411–414, doi: 10.1126/science.1105466.

Chengdu Institute of Geology and Mineral Resources China, Geological Survey, 2004. Geological Map of Qinghai-Xizang (Tibet) plateau and adjacent areas, In: Chengshu, W., Kedong, H. (Eds.). Chengdu Cartographic Publishing House, Chengdu.

Clark, M.K., Farley, K.A., Zheng, D., Wang, Z., Duvall, A.R., 2010. Early Cenozoic faulting of the northern Tibetan Plateau margin from apatite (U-Th)/He ages. Earth and Planetary Science Letters 296, 78.

Dupont-Nivet, G., Hoorn, C., Konert, M., 2008. Tibetan uplift prior to the Eocene-Oligocene climate transition: Evidence from pollen analysis of the Xining Basin. Geology 36, 987-990.

Dupont-Nivet, G., Horton, B.K., Butler, R.F., Wang, J., Zhou, J., Waanders, G.L., 2004. Paleogene clockwise tectonic rotation of the Xining-Lanzhou region, northeastern Tibetan Plateau. Journal of Geophysical Research-Solid Earth 109, doi:10.1029/2003JB002620.

Evensen, N.M., Hamilton, P.J., O'Nions, R.K., 1977. Rare earth abundances in chondritic meteorites. Geochimica et Cosmochimica Acta 42, 1199-1212.

Faure, M., Lin, W., Shu, L., Sun, Y., Sharer, U., 1999. Tectonics of the Dabieshan (eastern China) and possible exhumation mechanism of ultra high-pressure rocks. Terra Nova 11, 251-258.

Guillot, S., Garzanti, E., Baratoux, D., Marquer, D., Maheo, G., de Sigoyer, J., 2003. Reconstructing the total shortening history of the NW Himalaya. Geochemistry Geophysics Geosystems 4, 1064, doi:1010.1029/2002GC000484.

Guillot, S., Maheo, G., de Sigoyer, J., Hattori, K.H., Pecher, A., 2008. Tethyan and Indian subduction viewed from the Himalayan high- to ultrahigh-pressure metamorphic rocks. Tectonophysics 451, 225-241.

Hames, W. E., and S. Bowring (1994), An empirical evaluation of the argon diffusion geometry in muscovite, *Earth & Planetary Science Letter*, *124*, 161-169.

Harrison, T. M., et al. (1985), Diffusion of 40Ar in biotite: Temperature, pressure and compositional effect, *Geochim. Cosmochim. Acta*, *49*, 2461-2468.

Harrison, T.M., Copeland, P., Kidd, W.S.F., Yin, A., 1992. Raising Tibet. Science 255, 1663-1670.

Hilairet, N., 2002. Pétrographie et thermobarométrie sur des métapélites à grenat-staurotide du Nord-Ouest Tibet (Qiangtang). Unpublished master report. Université Lyon 1.

Jolivet, M., Brunel, M., Seward, D., Xu, Z., Yang, J., Malavieille, J., Roger, F., Leyreloup, A., Arnaud, N., Wu, C., 2003. Neogene extension and volcanism in the Kunlun Fault Zone, northern Tibet: New constraints on the age of the Kunlun Fault. Tectonics 22, doi: 10.1029/2002TC001428.

Kapp, P., DeCelles, P.G., Gehrels, G.E., Heizier, M., Ding, L., 2007. Geological records of the Lhasa-Qiangtang and Indo-Asian collisions in the Nima area of central Tibet. Geological Society of America Bulletin 119, 917-932.

Kapp, P., Yin, A., Harrison, T.M., Ding, L., 2005. Cretaceous-Tertiary shortening, basin development, and volcanism in central Tibet. Geological Society of America Bulletin 117, 865-878.

Kapp, P., Yin, A., Manning, C.E., Harrison, T.M., Taylor, M.H., Ding, L., 2003. Tectonic evolution of the early Mesozoic blueschist-bearing Qiangtang metamorphic belt, central Tibet. Tectonics 22, 1043, doi:1010.1029/2002TC001383.

Leloup, P. H., et al., 2011, Long-lasting intracontinental strike-slip faulting: new evidence from the Karakorum shear zone in the Himalayas, *Terra Nova*, *23*, 92-99.

Lin, W., Faure, M., Monie, P., Scharer, U., Zhang, L.S., Sun, Y., 2000. Tectonics of SE China: New insights from the Lushan massif (Jiangxi Province). Tectonics 19, 852-871.

Liu, Q., Avouac, J.P., Tapponnier, P., Zhang, G.W., 1991. Holocene and active faulting in western Qantang. Terra Nova Abstr. 3, 265.

Lovera, O.M., 1992. Computer-Programs to Model Ar-40/Ar-39 Diffusion Data from Multidomain Samples. Computers & Geosciences 18, 789-813.

Lovera, O.M., Richter, F.M., Harrison, T.M., 1989. 40Ar/39Ar geothermometry for slowly cooled samples having a distribution of diffusion domaine size. 94, 917-936.

Mattauer, M., Matte, P., Malavieille, J., Tapponnier, P., Maluski, H., Xu, Z.Q., Lu, Y.L., Tang, Y.Q., 1985. Tectonics of the Qinling Belt - Buildup and Evolution of Eastern Asia. Nature 317, 496-500.

Matte, P., Tapponnier, P., Arnaud, N., Bourjot, L., Avouac, J.P., Vidal, P., Liu, Q., Pan, Y., Wang, Y., 1996. Tectonics of Western Tibet, between the Tarim and the Indus. Earth and Planetary Science Letters 142, 311-316.

Molnar, P., Tapponnier, P., 1977. Active tectonics of Tibet. Journal of Geophysical Research 83, 5361-5375.

Norin, E., 1946. Geological exploration in western Tibet. Rep. from the Swedish exp. to the NW prov. China under the leadership of dr. SVEN HEDIN. Geology III, 7.

Pan, Y., Zheng, D., Zhang, Q., 1992. Introduction to integrated scientific investigation on Karakorum and Kunlun mountains. China Meterological Press, Beijing.

Paquette, J.L., Montel, J.M., Chopin, C., 1999. U-Th-Pb dating of the Brossasco ultrahigh-pressure metagranite, Dora-Maira massif, western Alps. European Journal of Mineralogy 11, 69-77.

Passchier, C.W., Trouw, R.A.J., 1996. Microtectonics. 289pp., Springer, Berlin.

Peltzer, G., Saucier, F., 1996. Present-day kinematics of Asia derived from geologic fault rates. Journal of Geophysical Research-Solid Earth 101, 27943-27956.

Raterman, N.S., Cowgill, E., Lin, D., 2007. Variable structural style along the Karakoram fault explained using triple-junction analysis of intersecting faults. Geosphere 3, 71-85.

Robinson, D.M., Dupont-Nivet, G., Gehrels, G.E., Zhang, Y.Q., 2003. The Tula uplift, northwestern China: Evidence for regional tectonism of the northern Tibetan Plateau during late Mesozoic-early Cenozoic time. Geological Society of America Bulletin 115, 35-47.

Robinson , A. C., 2009. Evidence against Quaternary slip on the northern Karakorum Fault suggests kinematic reorganization at the western end of the Himalayan–Tibetan orogen. E.P.S.L. 286, 158-170.

Roger, F., Arnaud, N., Gilder, S., Tapponnier, P., Jolivet, M., Brunel, M., Malavieille, J., Xu, Z.Q., Yang, J.S., 2003. Geochronological and geochemical constraints on Mesozoic suturing in east central Tibet. Tectonics 22, 1037, doi:1010.1029/2002TC001466.

Roger, F., Jolivet, M., Malavieille, J., 2010. The tectonic evolution of the Songpan-Garze (North Tibet) and adjacent areas from Proterozoic to Present: A synthesis. Journal of Asian Earth Sciences 39, 254-269.

Roger, F., Tapponnier, P., Arnaud, N., Schärer, U., Brunel, M., Xu, Z.Q., Yang, J.S., 2000. An Eocene magmatic belt across central Tibet: mantle subduction triggered by the Indian collision? Terra Nova 12, 102-108.

Rowley, D.B., Currie, B.S., 2006. Palaeo-altimetry of the late Eocene to Miocene Lunpola basin, central Tibet. Nature 439, 677-681.

Sengör, A.M.C., Okurogullari, A.H., 1991. The role of accretionnary wedges in the growth of continents: Asiatic exemple from Argand to plate tectonics. Eclogae Geologicae Helveticae 84, 535-597.

Shervai, J.W., 1982. Ti-V plots, the petrogenesis of modern, ophiolitic lavas. Earth and Planetary Science Letters 59, 101-118.

Sobel, E.R., Arnaud, N., 1999. A possible middle Paleozoic suture in the Altyn Tagh, NW China. Tectonics 18, 64-74.

Stesky, R.M., 1978. Mechanisms of High-Temperature Frictional Sliding in Westerly Granite. Canadian Journal of Earth Sciences 15, 361-375.

Sun, S.S., McDonough, W.F., 1989. Chemical and isotopics sytematics of oceanic basalts: implication for mantle composition and processes. In: Magmatism in ocean basins, Saunders A.D. and Norry M.J. (eds.). Geological Society of London Special Publication 42, 313-345.

Tapponnier, P., Zhiqin, X., Roger, F., Meyer, B., Arnaud, N., Wittlinger, G., Jingsui, Y., 2001. Oblique Stepwise Rise and Growth of the Tibet Plateau. Science 294, 1671-1677.

Tapponnier, P. and Molnar P., 1977. Active faulting and tectonics in China. J.G.R., vol. 82, 20, 2905-2930.

Tatsumi, Y., Hamilton, D.L., Nesbitt, R.W., 1986. Chemical characteristics of fluid phase released from a subducted lithosphere and origin of arc magmas: evidence from high-pressure experiments and natural rocks. J. Volcano. Geotherm. Res. 29, 293-309.

Treolar, P.J., Coward, M.P., 1991. Indian plate motion and shape: constraints on the geometry of the Himalaya orogen. 191, 189-198.

Valli, F., Leloup, P.H., Paquette, J.-L., Arnaud, N., Li, H., Tapponnier, P., Lacassin, R., Guillot, S., Liu, D., Deloule, E., Xu, Z., Mahéo, G., 2008. New U/Pb constraints on timing of shearing and long-term slip-rate on the Karakorum fault. Tectonics 27. doi:10.1029/2007TC002184.

Van der Beek, P., Van Melle, J., Guillot, S., Pecher, A., Reiners, P.W., Nicolescu, S., Latif, M., 2009. Eocene Tibetan plateau remnants preserved in the northwest Himalaya. Nature Geoscience 2, 364-368.

Wallis, S., Tsujimori, T., Aoya, M., Kawakami, T., Terada, K., Suzuki, K., Hyodo, H., 2003. Cenozoic and Mesozoic metamorphism in the Longmenshan orogen: Implications for geodynamic models of eastern Tibet. Geology 31, 745-748.

Yin, A., Rumelhart, P.E., Butler, R., Cowgill, E., Harrison, T.M., Foster, D.A., Ingersoll, R.V., Zhang, Q., Zhou, X.Q., Wang, X.F., Hanson, A., Raza, A., 2002. Tectonic history of the Altyn Tagh fault system in northern Tibet inferred from Cenozoic sedimentation. Geological Society of America Bulletin 114, 1257-1295.

Tables captions

Table 1: Whole rock analysis of mafic rocks

Table 2: U/Pb data

Table 3: Micas $^{40}Ar/^{39}Ar$ data.

Table 4: K1C20 Kf $^{40}Ar/^{39}Ar$ data.

Table 5: K1C21 Kf $^{40}Ar/^{39}Ar$ data.

Table 6: Geochronological data summary

Appendix captions

Appendix A 1: LA-ICPMS instrumentation and analytical method.

Appendix A 2: Ar/Ar instrumentation and analytical method.

Figure captions

Figure 1: Geological frame of NW Tibet. **(a)** Main active faults and major paleogeographic blocks of Tibet superimposed on SRTM DEM. BC: Bangong Co, LMCF: Lungmu Co fault, GF: Gozha fault, G: Gerze, L: Lungmu Co range, N: Nyima, Y: Yanghu, XU: Xijir Ulan. North Kunlun suture : Early Paleozoic, South ~~Location of~~Kunlun and Jinsha sutures: late Paleozoic – early Mesozoic, Nujiang suture: middle Mesozoic, Yarlung-Zangpo: Tertiary. Frame corresponds to the studied area ~~in the India-Asia collision zone.~~(Fig. 1b). White points indicate Cretaceous mafic volcanism (Kapp et al., 2005); **(b)** Schematic structural map of North-western Tibet Plateau. From Matte et al., (1996), Chengdu geological institute, (2004), modified from Landsat ETM+ image interpretation. Inset shows the location of ~~figure~~Fig. 2a.

Figure 2: **(a)** Structural map of the central Lungmu Co range. Map drawn from SPOT and Landsat ETM+ image interpretation and field observations. **(b)** Geological cross sections across the LMC range. Sections are located on Fig. 2a.

Figure 3: field observations. **(a)** View of the northern edge of the ~~LungMu~~Lungmu Co (LMC) range. Point of view shown on Fig. 2a. **(b)** Verticalized (Eocene?) red beds in the LMC fault zone (section A, Fig. 2a). **(c)** Steep E-W micaschist with horizontal stretching lineation in the LMC fault zone. Hammer gives scale (section A, Fig. 2a). **(d)** C/S structures in calcschists of the LMC fault zone (section A, Fig. 2a). View from above. Lens gives scale. **(e)** trace of the active LMC fault in quaternary sediments southwest of the Sum Xi Co. The two arrows labelled F show the fault trace while the two labelled T show an ~90 m offset of a strath terrace. Google earth image 34°29'30"N, 80° 04'E.

Figure 4: Plots of selected major elements versus MgO for the Lungmu Co ~~basic~~mafic rocks. Group (1): ◊, Group (2): ~~-;~~□; Group (3): ~~-.~~Δ.

Figure 5: Chondrite-normalized REE and MORB-normalized multi-element plots for the Lungmu Co ~~basic~~mafic rocks. Chondrite and MORB normalization values from Evensen et al. (1977) and Sun and McDonough (1989), respectively. Same symbols as in Fig. 4.

Figure 6: Plot of mobile (Sr~~, Rb~~) versus immobile ~~(Sm, Eu, Zr) or mobile (Ba)~~(Pr, Nd) elements. This diagram discriminate the effects of fractional crystallization and remobilization of LILE elements by fluids. Same symbols as in Fig. 4.

Figure 7: Plots of incompatible elements ratios versus transition elements. Same symbols as in Fig. 4.

Figure 8: Ti vs V discrimination diagram of Shervai (1982). IAT: Island rc Tholeiites, MORB: Mid Oceanic Ridge Basalts, BABB: Back-Arc Basin Basalt, OIB: Oceanic Island Basalt. Same symbols as in Fig. 4.

Figure 9: U/Pb data. **a & b)** K1C21, **c)** K1L17a,b; **d)** K1L23 and 24 **e)** K1L25; **f)** K1L26;. All data-point error ellipses are 2σ. See data in Table 2 abd Table 6.

~~Geochronologic constrains. **(a)** U/Pb Concordia diagram fro sample K1C21 from the leucocratic sheared granites. Points are scattered but suggest a late Paleozoic/Early Mesozoic emplacement and show a strong inheritance at ca. 2 Ga. Error bars at 2σ are smaller than point size. **(b)**~~**Figure 10:** Ar/Ar data **a)** $^{40}Ar/^{39}Ar$ results for muscovites and biotites. All ages are at 1σ including the error on J factor. Muscovite ages are plateaus Biotite age is a total fusion (TF) age. **b)** K1C20 Kf, **c)** K1C21 Kf. For b and c, age spectrum (black) of each sample is shown together with the one calculated for the best cooling history shown in Fig. 11 (thick grey line).

~~**(c)** Cooling history.~~**Figure 11:** Thermal history of the Lungmu Co range. K1C20 & 21 K-feldspar cooling patterns modelled assuming a multi-domain diffusion process developed by Lovera and co-workers (see references in the text). Modelling has tested various solutions by a Monte Carlo algorithm to assess the variance of the resulting best fits. Grey shaded area, are the distribution at 90% confidence intervals of the best-fit cooling histories. Inner black and open diamond lines are the median 90% confidence intervals of the best fit cooling history. ~~Age spectrum of both~~Closure temperature for other thermochronological systems as given in text. Note that the volcanic rocks probably ~~sample are shown in the inset with the age model corresponding to the best-fit cooling history shown by a thick grey line superimposed on the experimental spectra. Open boxes are the muscovites, black box biotites and grey boxes (U-Th)/He (van der Beek et al., 2009). Ranges~~intruded in country rocks cooler than the closure temperature. (U-Th)/He data from Van der Beek et al., (2009). Ages ranges reported for the India-Asia onset of collision and for timing of deformation in northern Tibet are shown for comparison. Two possible cooling paths are shown.